

THE INFRARED SPECTROSCOPY OF COMPACT POLYCYCLIC AROMATIC HYDROCARBONS CONTAINING UP TO 384 CARBONS

ALESSANDRA RICCA¹, CHARLES W. BAUSCHLICHER, JR.², CHRISTIAAN BOERSMA^{3,5},
ALEXANDER G. G. M. TIELENS⁴, AND LOUIS J. ALLAMANDOLA³

¹ Carl Sagan Center, SETI Institute, 189 Bernardo Avenue, Mountain View, CA 94043, USA; Alessandra.Ricca-1@nasa.gov

² Entry Systems and Technology Division, Mail Stop 230-3, NASA Ames Research Center, Moffett Field, CA 94035, USA; Charles.W.Bauschlicher@nasa.gov

³ Space Science Division, Mail Stop 245-6, NASA Ames Research Center, Moffett Field, CA 94035, USA;

Louis.J.Allamandola@nasa.gov, Christiaan.Boersma@nasa.gov

⁴ Leiden Observatory, Leiden University, P.O. Box 9513, NL-2300 RA, The Netherlands; tielens@strw.leidenuniv.nl

Received 2011 November 23; accepted 2012 May 18; published 2012 July 6

ABSTRACT

The mid- and the far-infrared spectra of polycyclic aromatic hydrocarbons (PAHs) have been computed using density functional theory. This study has focused on PAHs in the highly symmetric, compact, coronene family with sizes up to 384 carbons. We have identified trends in the peak position and intrinsic strength of the vibrational modes of these species and compared these to trends previously reported for less symmetric and smaller PAHs. The computed spectral modes have been used to calculate the IR emission spectrum of PAHs pumped by UV photons. The results have been compared to observed interstellar spectra to elucidate the characteristics of the interstellar PAH family. The calculations show that highly symmetric PAHs are very stable and, hence, might be favored under the harsh conditions of interstellar space. Our calculated vibrational properties confirm and extend previous studies for small PAHs to the large compact PAHs studied here, specifically in terms of the dependence of the spectral characteristics on ionization and on H-adjacency. The calculations show that for PAHs larger than 150 carbons, the 6.3 μm feature becomes very broad and shifts to longer wavelengths, the 8.6 μm band becomes stronger than the “7.7” μm band, and the 11.0/12.7 band strength ratio gets too large compared with observations. Thus, PAHs with 150 carbons or more are unlikely to be the dominant species in interstellar space. The simplicity of the observed spectra in the 15–20 μm range points toward a preponderance of compact PAHs in the interstellar PAH family.

Key words: astrochemistry – infrared: general – methods: numerical – molecular data

Online-only material: color figures

1. INTRODUCTION

The spectra of a wide variety of objects with associated gas and dust show strong mid-infrared emission with discrete emission features at 3.3, 6.2, “7.7,” 8.6, 11.2, and 12.7 μm as well as a host of weaker bands. Ground-based and space-based observations have shown that these infrared emission features are ubiquitous characteristics of the mid-infrared spectra of H II regions, post-AGB stars, planetary nebulae, young stellar objects, infrared cirrus, the interstellar medium (ISM) of galaxies, galactic nuclei, and ultraluminous infrared galaxies (Geballe et al. 1989; Verstraete et al. 1996; Moutou et al. 1999; Hony et al. 2001; Meeus et al. 2001; Peeters et al. 2002; Regan et al. 2004; Engelbracht et al. 2006; Armus et al. 2007; Sloan et al. 2005; Smith et al. 2007; Sellgren et al. 2007). These emission features are very characteristic for the vibrational modes of polycyclic aromatic hydrocarbon (PAH) molecules (Léger & Puget 1984; Allamandola et al. 1985, 1989) and, because these emission features are bright even far from the illuminating stars and in the general diffuse ISM, molecular-sized carriers containing ≈ 50 –100 carbons are indicated (Sellgren 1984). Essentially, molecular-sized PAHs are very efficient absorbers of UV radiation, but have only a limited heat capacity and they are transiently heated to high temperatures. The absorbed energy is rapidly distributed over the vibrational levels and the molecule relaxes radiatively through vibrational IR emission. The infrared emission features are thus the consequence of a

fluorescence process when the emitters are very warm after the absorption of a UV photon. For a recent review of the properties of interstellar PAHs, see Tielens (2008).

The IR emission features are generally perched on top of broad emission plateaus whose strength varies independently (Bregman et al. 1989; Peeters et al. 2002). The underlying plateaus have been attributed to larger PAHs and/or PAH clusters containing ≈ 400 carbons (Bregman et al. 1989) which are also fluorescing but do not get that warm upon absorption of a UV photon. In addition, the mid-IR spectra reveal the presence of an underlying continuum that sharply rises toward longer wavelengths. This continuum is likely related to the mid-IR cirrus first discovered by *IRAS* in the mid-1980s (Low et al. 1984). The carrier of this continuum also fluctuates in temperature, but the emitting species are larger—some thousands of atoms—and the resulting temperature excursions more limited (Desert et al. 1990; Draine & Li 2001). It seems therefore that PAH molecules are merely the extension of the interstellar grain size distribution into the molecular domain.

Previous observations with the *Infrared Space Observatory* (*ISO*) and the *Spitzer Space Telescope* have focused on the mid-IR, but the *Herschel Space Observatory* and the Stratospheric Observatory for Infrared Astronomy (*SOFIA*) are poised to open up the far-IR to systematic spectroscopic searches for the long-wavelength counterparts of the PAH features (Joblin et al. 2011). The far-IR is the domain of PAH skeletal vibrations involving the whole molecule, and long-wavelength emission features have great potential to provide insight into the size and shape of the emitting species (Mulas et al. 2006a; Mattioda

⁵ NASA Postdoctoral Program.

et al. 2009; Ricca et al. 2010; Boersma et al. 2011). Because long-wavelength emission is dominated by cooler species, far-IR features potentially probe preferentially the large end of the astronomical PAH distribution. Studies of the spectroscopic properties of PAHs, particularly of large species, will be key to planning such observational searches.

Much progress has been made over the last decade in determining the intrinsic spectral properties of PAH molecules due to the dedicated efforts of a number of laboratory groups using a variety of complementary experimental techniques (Szczepanski & Vala 1993a; Schlemmer et al. 1994; Moutou et al. 1996; Cook et al. 1998; Piest et al. 1999; Hudgins & Allamandola 1999a, 1999b; Oomens et al. 2001, 2003; Kim et al. 2001). Each of these techniques has its advantages and disadvantages. These have been critically reviewed by Oomens (2011). These experimental studies have focused primarily on PAH molecules which are small—typically 10–32 C-atoms—compared to the estimated sizes of PAHs in space, as large PAHs have low vapor pressures and are hence difficult to study in the gas phase. These experimental studies have benefited much from the guidance of theoretical calculations using density functional theory (DFT) and, over the years, extensive studies have been made (de Frees et al. 1993; Langhoff 1996; Mallocci et al. 2007; Pathak & Rastogi 2007; Bauschlicher et al. 2008, 2009, 2010; Ricca et al. 2010). Such theoretical studies are only limited by computer speed, and Moore’s law has led to a steady increase in the maximum size PAH that can be calculated. Presently, the IR vibrational harmonic modes of highly symmetric closed-shell PAHs approaching 400 C-atoms can be calculated. The theoretical approach has the added advantage that the molecular structure of the PAH can be easily systematically varied and trends can be evaluated in detail. For example, previously, theoretical calculations have provided the mid- and far-infrared spectra for neutral and charged PAHs (Mallocci et al. 2007; Pathak & Rastogi 2007; Bauschlicher et al. 2010) as well as size-dependent PAHs spectra between 10 and 130 carbons and spanning both compact and eroded shapes (Langhoff 1996; Bauschlicher et al. 2008, 2009; Ricca et al. 2010). These experimental and theoretical studies have been widely used in the development of astronomical models to guide the adopted intrinsic properties of the emitting interstellar PAH family (Desert et al. 1990; Schutte et al. 1993; Draine & Li 2001). Such models are of course only as good as the experimental and theoretical studies of PAH properties allow.

Interpretation of the observations will rely on a thorough understanding of the spectroscopic properties of large PAHs, clusters, and very small grains, as a function of charge, size, and shape. Here, we use DFT to perform a systematic study of the vibrational spectra of a set of PAH molecules as a function of size. We focus here on the highly symmetric coronene family, which allows us to probe a very large size range (24–384 C-atoms) methodically. PAHs within this family are expected to be exceedingly stable and have often been considered prime templates for the interstellar PAH family. Because the effect of charge is known to be large for (small) PAHs, we include in our studies neutrals as well as PAH cations/anions. However, because charging lowers the symmetry, the maximum size of PAH ions is more limited (up to about 200 C-atoms). With the advent of SOFIA and *Herschel*, there is also an increased need for the far-infrared spectra of large PAHs. This paper is laid out as follows. In Section 2, we describe our theoretical method. The results of our calculations for the intrinsic IR characteristics of the coronene family are presented and compared to results of

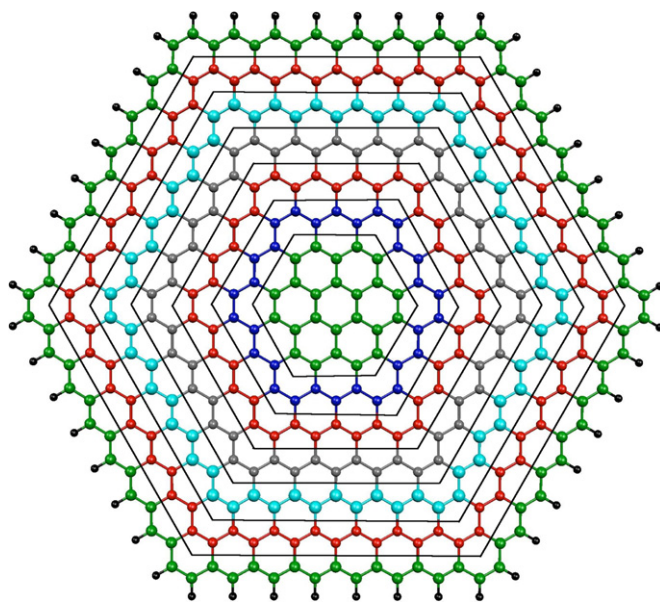


Figure 1. Superimposed structures of the PAHs considered in this work. The carbon framework for each molecule is enclosed in a hexagon. Starting from the inner molecule, $C_{24}H_{12}$ (green), PAHs are built by adding an additional set of rings around the outside. In such a way, the following PAHs are obtained: $C_{54}H_{18}$ (dark blue edge), $C_{96}H_{24}$ (red edge), $C_{150}H_{30}$ (gray edge), $C_{216}H_{36}$ (light blue edge), $C_{294}H_{42}$ (red edge), and $C_{384}H_{48}$ (green edge). (A color version of this figure is available in the online journal.)

previous studies in Section 3, which starts with a discussion of the calculated stability of PAHs. The astronomical implications of our study are presented in Section 4. Finally, our results are summarized and our conclusions are presented in Section 5.

2. MODEL AND METHODS

We have investigated several families of compact PAHs: the “coronene,” the “ovalene,” the “anthracene,” and the “tetracene” families. These families are obtained by adding a complete ring of hexagons around a central unit, namely benzene for the coronene family, naphthalene for the ovalene family, anthracene for the anthracene family, and tetracene for the tetracene family. The members of the coronene family are shown in Figure 1. We only report a detailed description of the spectroscopic properties of the coronene family in Section 3.2, however, in Section 4, we include all of the families in the analysis. The spectroscopic properties of the ovalene, anthracene, and tetracene families will be published in a separate publication.

All of the neutral species of the coronene family have D_{6h} symmetry. Since the highest occupied and lowest unoccupied orbitals of the neutral are degenerate, removing or adding an electron to form the cation and anion leads to a lowering of the molecular symmetry due to the Jahn–Teller effect. In D_{6h} symmetry, the ground electronic states of cations and anions are either ${}^2E_{1g}$ or ${}^2E_{2u}$. The direct product $e_{1g} \times e_{1g}$ or $e_{2u} \times e_{2u}$ is $a_{1g} + a_{2g} + e_{2g}$. Since a_{1g} and a_{2g} vibrations do not lift the degeneracy, only the e_{2g} modes are Jahn–Teller active. The e_{2g} modes are forbidden in D_{6h} , but are allowed in the lower symmetry. The Jahn–Teller stabilization is small for large PAHs, for example 140 cm^{-1} for $C_{96}H_{24}^+$. The computed harmonic spectra of the two lower symmetry states are very similar, excluding the mode that interconverts the two states. On the basis of these factors, we conclude that the strongly allowed transitions, which are not Jahn–Teller active, should be well described by our scaled harmonic frequencies for the full width

at half-maximum (FWHM) used in this work. This conclusion is supported by the agreement between theory and experiment (Hudgins & Allamandola 1995) for the band positions of the three bands observed in experiment for the coronene cation. The previously forbidden e_{2g} modes will be less accurate due to the neglect of Jahn–Teller effects, but these bands are expected to be weak and are not considered in detail in this work.

All of the DFT calculations were performed using Gaussian 09 (Frisch et al. 2009) and earlier versions. The interactive molecular graphics tool MOLEKEL (Portmann & Lüthi 2000) was used to aid the analysis of the vibrational modes. The structures were fully optimized and the harmonic frequencies computed using DFT. We used the hybrid B3LYP (Becke 1993; Stephens et al. 1994) functional in conjunction with the 4-31G basis set (Frisch et al. 1984). Previous work (Bauschlicher & Langhoff 1997) has shown that the computed B3LYP/4-31G harmonic frequencies scaled by a single scale factor of 0.958 are in excellent agreement with the matrix isolation mid-infrared fundamental frequencies of the PAH molecules. Joblin et al. (2002) and Mulas et al. (2006a) found that the mid-infrared scale factor was reasonable for the far-infrared bands. A far-infrared study of neutral coronene, ovalene, and dicoronylene (Mattioda et al. 2009) also showed that the mid-infrared scale factor of 0.958 can be applied to the far-infrared spectral region as it brings the computed B3LYP/4-31G harmonic frequencies into excellent agreement with the experimental far-infrared frequencies. The scale factor to bring the computed bands in the 15–20 μm range for 13 large molecules into the best agreement with experiment is essentially 0.958 as well (Boersma et al. 2010). Therefore, in the present work, we use the scale factor of 0.958 for all bands.

We do not consider overtones, combination bands, and resonances (Fermi for example). The overtones and combination bands are expected to be weak and therefore significantly less important than the fundamental frequencies in explaining the major features of the observed spectra. While ignoring resonances might affect the shape of the spectra of one molecule, it is unlikely that a resonance will affect all members of a family in the same manner. Therefore, the overall trends that our spectra show should be valid. Supporting our neglect for resonances is the experimental spectra of Huneycutt et al. (2004) for the C–H stretching region of several PAHs, where the experimental spectra were found to be in good agreement with DFT calculations. That is, theory and experiment agreed even for C–H stretching bands that have by far the largest anharmonic effects. We should also note that we use a sizable FWHM which helps to mask many of these finer details.

We only consider principal isotopes and do not include the effect of isotopic substitutions. We should note that the effect of substituting a ^{13}C for a ^{12}C is small. For neutral $\text{C}_{96}\text{H}_{24}$, we find that spectra where all of the carbons are ^{12}C s and the ten spectra created by replacing each of the ten unique carbons with a ^{13}C are so similar that the small differences between them are hardly visible. The effect of deuteration is larger, but has been discussed previously (see, for example, Hudgins et al. 2004) and is not reported here.

Previous work has shown that the band intensities are in reasonably good agreement with experiment in the 5–20 μm range (see Mattioda et al. 2009 and reference therein). Some discrepancies exist for the C–H stretching mode in small PAHs (Langhoff 1996). However, it is not clear that this extends to large PAHs as well and therefore we present and use the computed intensities without any modification.

The computed spectra are for absorption. However, astronomical PAHs are not typically observed in absorption. After absorbing a photon, the electronic excited state crosses to the ground state potential and infrared emission occurs from these vibrationally hot ground electronic state molecules (Allamandola et al. 1989; Leach 1989; Puget & Léger 1989). Due to molecular anharmonicity and the level of excitation, this emission is shifted to the red compared with absorption (e.g., Joblin et al. 1995; Oomens et al. 2003). It is possible to compute the anharmonic corrections for small molecules from numerical differences of analytic second derivatives (see, for example, Barone 2005) or from molecular dynamic simulations (see, for example, Van-Oanh et al. 2012), but these approaches are computationally very expensive and only practical for small molecules. While shifts have not been measured or computed for large molecules, a redshift of 15 cm^{-1} is a reasonable choice; see, for example, Bauschlicher et al. (2009).

In Section 3.2, absorption spectra are presented and the values in the text and in the tables are not shifted by 15 cm^{-1} . However, the shift is applied in many of the figures where comparisons with astronomical spectra are made (as noted in their captions). In Section 4, comparisons with observations are made and the shift is applied to the computed spectra and to the values reported in the text.

To aid comparison with astronomical spectra, we have to broaden our computed results. Ideally, one would like to vary line width as a function of mode, but this is not practical; therefore, we vary the line width with the wavelength. A width (FWHM) of 30 cm^{-1} is taken for the bands shortward of 10 μm , while a line width of 10 cm^{-1} is used for the bands between 10–15 μm , because these values are consistent with current observational and theoretical modeling (see discussion in Bauschlicher et al. 2009). An FWHM of 5 cm^{-1} is used in the region 15–20 μm to be consistent with the observations that line widths in this region are 4–8 cm^{-1} (e.g., van Kerckhoven et al. 2000; Moutou et al. 1998). For 20–1000 μm , we expect the FWHM to decrease with increasing wavelength, and we assume a linear scaling in wavenumber space from 5 for 500 cm^{-1} (20 μm) to 0.5 cm^{-1} for 1 cm^{-1} (1000 μm). At the longer wavelengths, PQR rotational band envelopes are expected (Mulas et al. 2006a, 2006b), but this refinement is not incorporated here. Despite these limitations, these idealized spectra can be useful in better understanding the PAH population and astronomical spectra.

The computational studies yield integrated band intensities in km mol^{-1} , which we broaden in wavenumber space as described above. The units on the y -axis in the figures shown here are given as a cross section, which has units of $10^5 \text{ cm}^2 \text{ mol}^{-1}$. For wavelengths shorter than 20 μm , the x -axis is linear in μm to be consistent with how observational results are commonly presented. For wavelengths longer than 20 μm , the x -axis is linear in cm^{-1} to better display the entire region in a single plot.

The computational cost of these PAH DFT harmonic frequency calculations depends on many factors, such as the symmetry of the molecule, whether the systems have a closed or open-shell structure, and even on the available computer memory, which affects whether quantities need to be recomputed or not. For the closed-shell neutral species $\text{C}_{96}\text{H}_{24}$ to $\text{C}_{294}\text{H}_{42}$, we find that the cpu time grows approximately as the number of carbons to the power of 2.1. Due to memory limitations, our time jumps for $\text{C}_{384}\text{H}_{48}$ and therefore it does not follow the trend of the smaller molecules. The calculation of the harmonic

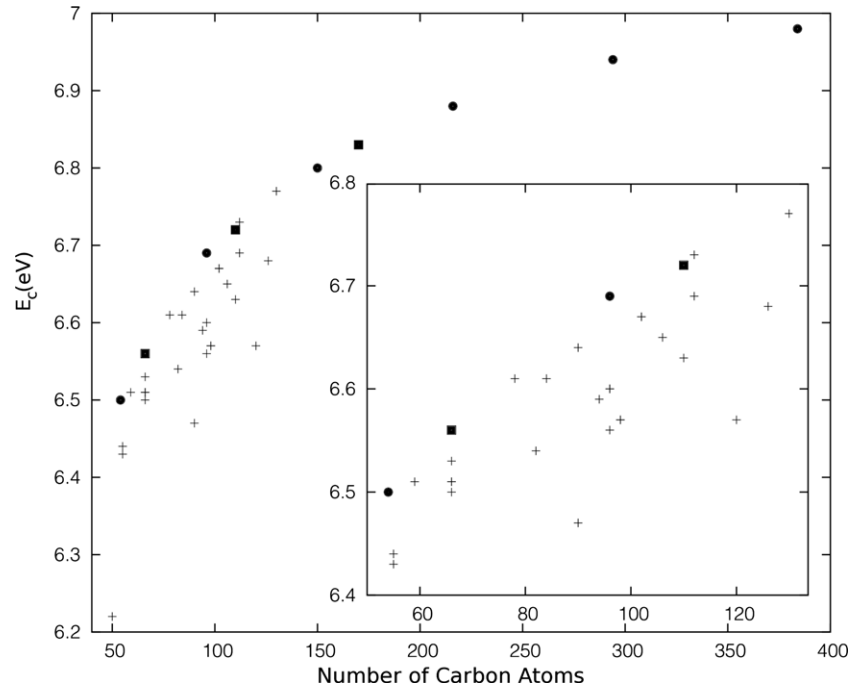


Figure 2. Binding energies per carbon, E_c (in eV), as a function of the number of carbons. E_c is defined in Equation (1). The coronene family is plotted with filled circles, the ovalene family with filled squares, and the remaining PAHs are plotted with plus symbols.

frequencies for $C_{216}H_{36}$ had an elapsed time of about two days on a workstation with four processors per cpu, while the calculation for the lower symmetry $C_{216}H_{36}$ cation required about 80 times longer. Thus, even with the constant improvement in computer power, it will be a few years before calculations of this size or larger become routine.

3. RESULTS AND DISCUSSION

This section is presented in two parts. Part one (Section 3.1) gives an overview of the thermodynamic stabilities of many large PAHs of various shapes, which were obtained computationally from the molecules studied in this work or from data included in the NASA Ames PAH IR Spectroscopic Database (Bauschlicher et al. 2010). Part two (Section 3.2) presents and discusses the infrared spectroscopy of a subset of the most stable of these PAHs, namely, the members of the coronene family up to $C_{384}H_{48}$ (see Figure 1).

3.1. PAH Stability

To truly assess the stability of these species in the ISM, one would have to compute the energy required to remove fragments from a PAH edge, which would represent a large undertaking. However, some insight into the relative stabilities of the PAHs can be obtained by computing the average binding energies per carbon, E_c , which have been computed using DFT for PAHs with various shapes and sizes and which are summarized in Figure 3 and shown graphically in Figure 2. For a PAH with the formula C_nH_m , E_c is defined as

$$E_c = (AE - m \times D_e(C-H))/n, \quad (1)$$

where AE is the atomization energy, i.e., the energy required to separate the C_nH_m molecule into n carbon atoms and m hydrogen atoms, and $D_e(C-H)$ is the average C–H bond energy. Because the loss and reformation of C–H bonds are expected to occur as a function of time, we have subtracted the C–H bond energies to focus only on the stability of the C skeleton.

The plot of E_c as a function of PAH size (see Figure 2) shows a rapid increase in average carbon binding energy with size for PAHs having from 50 up to roughly 120–150 carbon atoms. After about 120 carbon atoms, the E_c value grows more slowly with increasing PAH size, asymptotically approaching the value for an infinite graphene sheet (7.3 eV) computed at the same level of theory.

The binding energies per carbon atom for the PAHs reveal that the structures with the highest stability for a given number of carbon atoms are compact, almost circular in shape. Among these are $C_{54}H_{18}$, $C_{96}H_{24}$, $C_{150}H_{30}$, $C_{216}H_{36}$, $C_{294}H_{42}$, and $C_{384}H_{48}$, all members of the “coronene” family, having structures that are obtained by sequentially adding a ring of benzenes around a central coronene unit (see Figure 1). The enhanced stability of such highly condensed PAH structures was already surmised by Stein (1978) based upon a simple group-additive predictive scheme of thermodynamic stability. If protruding hexagonal rings are added to the corners of these compact PAHs, although they grow in size, their stability drops. For example, adding six rings to the corners of circumcoronene ($C_{96}H_{24}$) to form the snowflake-shaped $C_{120}H_{36}$ lowers E_c by 0.12 eV. These types of pendent rings carry quartet hydrogens. Adding protruding rings along the PAH sides instead of the corners has less dramatic effects on E_c as shown for $C_{102}H_{26}$. This PAH is formed by adding two rings to $C_{96}H_{24}$ that introduce only trio hydrogens, not quartet hydrogens. The difference in E_c between $C_{96}H_{24}$ and $C_{102}H_{26}$ is only 0.02 eV. This suggests that growth by adding rings that introduce quartet hydrogens to the PAH structure reduces E_c more than the addition of rings that add trio hydrogens. This conclusion is in contrast to the Hückel results of Stein & Brown (1987), who found that large compact PAHs with only solo and duo hydrogens were less stable than compact-based structures containing trio and quartet hydrogens along their edges. Given the high level of accuracy of hybrid DFT methods for heats of formations, we are confident that our DFT results are much superior to those obtained by Stein and Brown using a semiempirical approach. Creating a hole in the center of a compact PAH

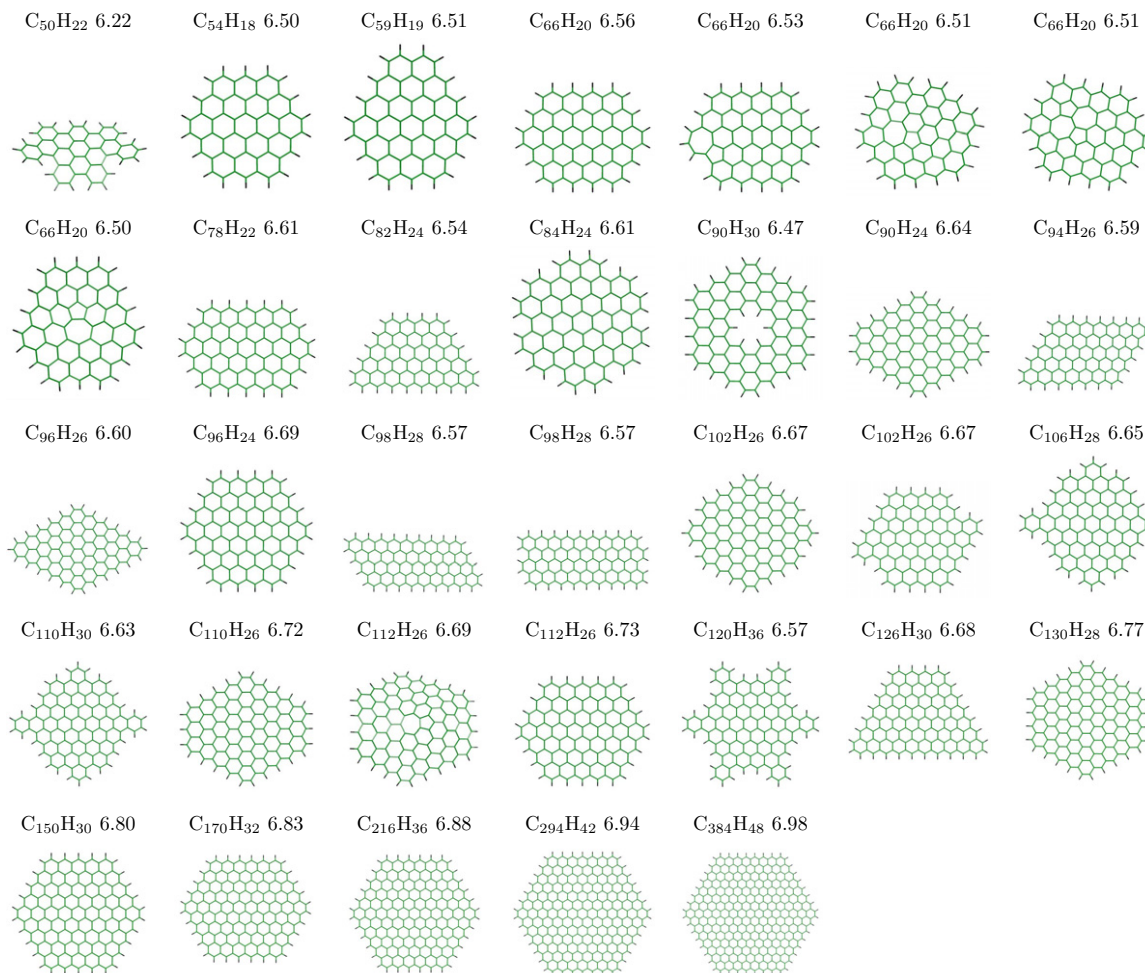


Figure 3. Binding energies per carbon, E_c , in eV.
(A color version of this figure is available in the online journal.)

has a dramatic effect on the stability. For example, the E_c value for $C_{90}H_{30}$ is 0.22 eV less than for $C_{96}H_{24}$.

Compact PAHs with elliptical shapes have E_c values similar to those for the “coronene” family. Figure 2 shows that the E_c values for the “ovalene” family, namely $C_{66}H_{20}$, $C_{112}H_{26}$, and $C_{170}H_{32}$, fall on the same stability line as for the “coronene” family. Defects, such as five- and seven-membered rings, reduce the PAH stability depending on their position in the carbon skeleton (compare the results for $C_{66}H_{20}$ with defects to the parent without any defects), but they do not affect their infrared spectra (Ricca et al. 2011b). Comparing carbon binding energies for PAHs of comparable sizes in Figure 3 shows that the lowest stabilities are those with trapezoidal ($C_{82}H_{24}$ and $C_{126}H_{30}$), parallelogram ($C_{94}H_{26}$ and $C_{98}H_{28}$), rectangular ($C_{98}H_{28}$), and rhomboidal ($C_{96}H_{26}$) shapes, all containing sharp corners with trio hydrogens.

The average bond energies yield some insight into the relative stabilities of the PAHs. First, the PAHs with “smooth” edges have similar stabilities as a function of size; that is, the oval PAHs and spherical PAHs are expected to have very similar stabilities in the ISM. The PAHs with pendent rings containing trio and quartet hydrogens are less stable than the smoothed edge PAHs. It is extremely likely that the core of the “bumpy” PAHs have a stability similar to that of the core of smooth PAHs of the same size, thus the reduction in the average bond energy must be due to the pendent rings. Consider $C_{120}H_{36}$ vs. $C_{96}H_{24}$;

if one assumes that the 96 core carbons of $C_{120}H_{36}$ have the same average bond energy as $C_{96}H_{24}$, then the average bond energy of the six pendent rings must be about 0.6 eV smaller. This difference is sufficiently large that it seems safe to conclude that it is more likely to remove the pendent rings to make a smooth PAH than to roughen the edges of the smooth PAHs of similar size. A similar conclusion would apply to species with defects at the edge. However, it is more difficult to assess how defects in the center affect the stability in the ISM as the destruction mechanism for a PAH with defects in the center is not obvious. Thus, while the average bond energy is not a perfect measure of the stability in the ISM, these results strongly support the view that very compact PAHs, such as the those in the coronene and ovalene families, are exceedingly stable, and hence are expected to be more resistant to destructive processes in the harsh environment of the ISM (Micelotta et al. 2010).

3.2. Infrared Spectroscopy of the Coronene Family

This discussion is broken up in the following wavelength regions: the 2.5–3.5 μm region, which is dominated by the C–H stretching (CH_{str}) fundamental; the 6–10 μm region, which is associated with the CH_{str} and C–H in-plane (CH_{ip}) bending vibrations; the 10–15 μm region, which spans the C–H out-of-plane (CH_{oop}) bending modes; the 15–20 μm region, where the vibrational modes transition from those characterized by

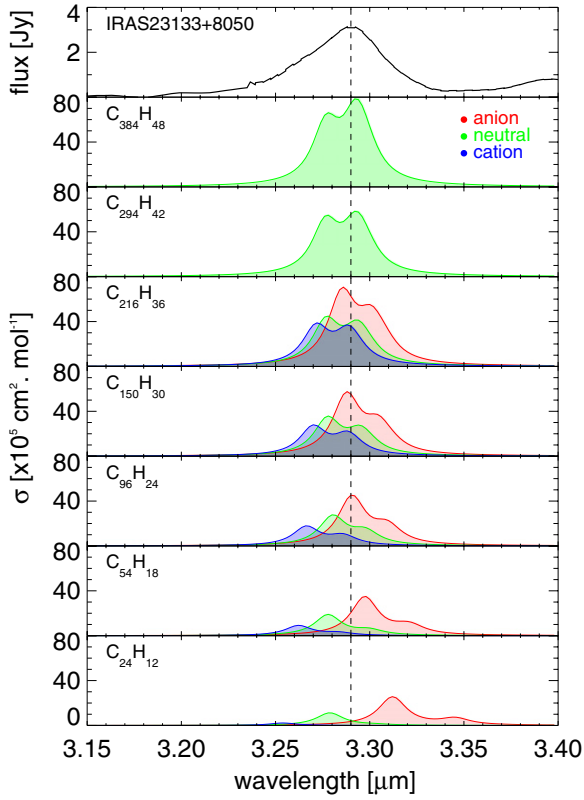


Figure 4. Absorption spectra in the $3\ \mu\text{m}$ region for the neutral and charged species of the coronene family, redshifted by $15\ \text{cm}^{-1}$. An FWHM of $16\ \text{cm}^{-1}$ is used to show the decomposition of the solo and duo stretches. For comparison, the top panel shows the observed spectrum of the prototypical class A source, IRAS 23133+6050, over the same wavelength region (Peeters et al. 2002). A dashed line is drawn at the maximum ($3.29\ \mu\text{m}$) in the observed spectrum. (A color version of this figure is available in the online journal.)

Table 1

C–H Band Position Maximum (in μm), Total Intensity (in km mol^{-1}), and Intensity per C–H (in $\text{km mol}^{-1}\ \text{H}^{-1}$)

Molecule	Cation			Neutral			Anion		
	λ	I	$I(\text{CH})$	λ	I	$I(\text{CH})$	λ	I	$I(\text{CH})$
$\text{C}_{24}\text{H}_{12}$	3.240	57.6	4.8	3.263	296.4	24.7	3.298	787.3	65.5
$\text{C}_{54}\text{H}_{18}$	3.249	285.9	15.9	3.264	576.3	32.0	3.284	1077.6	59.9
$\text{C}_{96}\text{H}_{24}$	3.256	629.5	26.2	3.268	931.3	38.8	3.279	1479.9	61.7
$\text{C}_{150}\text{H}_{30}$	3.261	1083.3	36.1	3.268	1349.2	45.0	3.276	2008.5	66.9
$\text{C}_{216}\text{H}_{36}$	3.264	1610.2	44.7	3.269	1838.4	51.1	3.275	2654.8	73.7
$\text{C}_{294}\text{H}_{42}$				3.270	2409.5	57.4			
$\text{C}_{384}\text{H}_{48}$				3.271	3072.4	64.0			

Note. No redshift is applied.

molecular sub-group motions to macroscopic motions; and the 20–3000 μm region, where the motion is that of the entire molecule acting in unison.

3.2.1. The C–H Stretching Vibrations (2.5–3.5 μm)

A summary of the unshifted C–H band position maxima, λ , total intensities, I , and intensities per C–H, $I(\text{CH})$, for the neutral and charged PAH members of the coronene family is presented in Table 1. The redshifted absorption spectra of this region are shown in Figure 4. Note that the adopted FWHM is $16\ \text{cm}^{-1}$ to reveal addition features in these bands. The results are in agreement with previous work by Bauschlicher et al. (2008). The band positions for the neutrals are fairly insensitive

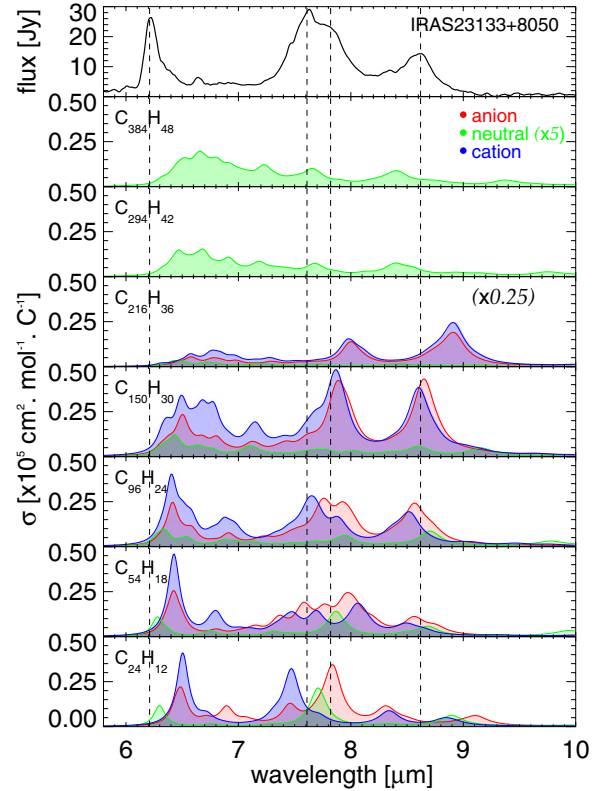


Figure 5. The 6–10 μm region of the spectra for the species studied in this work. A redshift of $15\ \text{cm}^{-1}$ is used. For comparison, the top panel shows the observed spectrum of the prototypical class A source, IRAS 23133+6050, over the same wavelength region (Peeters et al. 2002). Dashed lines have been added at the dominant peaks of the observed spectra, at 6.21, 7.61, 7.82, and 8.62 μm . The cross sections have been normalized to the number of carbon atoms to limit the dynamic range. (A color version of this figure is available in the online journal.)

to PAH size and the intensity per C–H increases with size. For PAH cations, the peak positions shift to longer wavelengths as the PAHs get larger. Upon ionization, the intensity per C–H of $\text{C}_{24}\text{H}_{12}$ drops by a factor of five. Pauzat et al. (2010) have discussed this change in intensity between the neutral and cation in terms of σ and π orbital occupations, while Schmidt et al. (2009) gave an equivalent description in terms of a competition between charge, charge flux, and dipole flux terms. As the PAH size increases, the cation charge is spread over an increasing number of carbons, which reduces the difference between the neutral and the cation charge and charge flux terms (Schmidt et al. 2009); this reduces the difference in the intensity per C–H, $I(\text{CH})$, between the cation and neutral with increasing PAH size. For example, for $\text{C}_{54}\text{H}_{18}^+$, $I(\text{CH})$ decreases by a factor of two compared to the neutral, for $\text{C}_{96}\text{H}_{24}^+$ $I(\text{CH})$ decreases by a factor of 1.48, and for $\text{C}_{150}\text{H}_{30}^+$ it decreases by a factor of 1.25. Clearly, large PAH cations and neutrals have comparable intensities. For the anions, the effect of charge is less pronounced. The band position is not very affected by the increase in PAH size. If we exclude $\text{C}_{24}\text{H}_{12}^-$, then the intensity per CH increases with size, but much more slowly than for the neutrals and cations.

3.2.2. The C–C Stretching and C–H In-plane Bending Vibrations (6–10 μm)

The PAH bands in this region of the spectrum correspond to C–C stretching (CC_{str}) and C–H in-plane bending (CH_{ip}) vibrations as shown in Figure 5 (n.b. the bands have been redshifted for comparison with observations). As with all earlier

studies, the intensities of the major features between 5.5 and 10 μm are enhanced by an order of magnitude or more upon ionization. In general, the pure CC_{str} falls between 6.35 and 6.45 μm , the strongest PAH bands produced by coupled CC_{str} and CH_{ip} bending vibrations fall between 7–8 μm , while the bands due to CH_{ip} bending vibrations fall between 8 and 9 μm . Small PAHs, such as $\text{C}_{24}\text{H}_{12}$ and $\text{C}_{54}\text{H}_{18}$, have a single peak in the pure CC_{str} region (6.2–6.5 μm). For neutral $\text{C}_{24}\text{H}_{12}$ and $\text{C}_{54}\text{H}_{18}$, the pure CC_{str} bands peak at 6.239 and 6.226 μm , respectively, and shift to longer wavelengths for the ions, namely 6.442 μm for $\text{C}_{24}\text{H}_{12}^+$, 6.418 μm for $\text{C}_{24}\text{H}_{12}^-$, 6.365 μm for $\text{C}_{54}\text{H}_{18}^+$, and 6.364 μm for $\text{C}_{54}\text{H}_{18}^-$. As the PAH size increases, the spectra in the 6.5–7.5 μm region become more complex with more distinct peaks that eventually blend to form a broad feature. The pure CC_{str} falls at 6.266 μm for $\text{C}_{96}\text{H}_{24}$, 6.366 μm for $\text{C}_{150}\text{H}_{30}$, 6.387 μm for $\text{C}_{216}\text{H}_{36}$, 6.406 μm for $\text{C}_{294}\text{H}_{42}$, and 6.446 μm for $\text{C}_{384}\text{H}_{48}$. For the ions containing up to 96 carbons, the position of the CC_{str} feature is rather insensitive to PAH size. For $\text{C}_{150}\text{H}_{30}^+$ and $\text{C}_{150}\text{H}_{30}^-$, the pure CC_{str} band becomes part of a broad feature that spans from 6.2 to 7.5 μm .

The features present in the 6.5–8.0 μm region are due to in-plane CC_{str} modes, which couple with CH_{ip} bending modes. As the PAH size increases, the number of C–C and C–H bonds increases and so does the number of ways the C–C and C–H modes can couple together, which produces an increasing number of features in the 6.5–7.5 μm region. For $\text{C}_{384}\text{H}_{48}$, this results in a very broad absorption peak with maximum intensity at 6.6 μm .

The strongest band near 7.7 μm varies in position depending on PAH size and charge. For the neutrals, except for $\text{C}_{54}\text{H}_{18}$ and $\text{C}_{96}\text{H}_{24}$, the band falls between 7.634 μm for $\text{C}_{150}\text{H}_{30}$ and 7.570 μm for $\text{C}_{384}\text{H}_{48}$. For small PAHs, the cation band usually falls at a shorter wavelength than the neutral and the anion at a longer wavelength than the neutral. As the PAH size reaches 150 carbons, the spectra of the cation and of the anion look similar, with the “7.7” μm feature centered at 7.777 μm for the cation and at 7.805 μm for the anion. The “7.7” μm feature becomes more intense than the 6.5 μm feature for $\text{C}_{150}\text{H}_{30}^+$ and $\text{C}_{150}\text{H}_{30}^-$.

We now focus on the dominant band between 8.0 and 8.75 μm , i.e., the feature closest to the interstellar “8.6” μm band. The peak position is quite dependent on the PAH size and converges to 8.610 μm for neutral $\text{C}_{384}\text{H}_{48}$. This feature is less dependent on PAH size for the ions, falling at 8.496 for $\text{C}_{150}\text{H}_{30}^+$ and at 8.541 for $\text{C}_{150}\text{H}_{30}^-$. Neutral PAHs show a band between 9 and 10 μm that arises from CH_{ip} bending motions which are coupled with CC -skeletal motions. The position of this peak does not follow a specific trend with PAH size. This peak carries no intensity for the ions.

3.2.3. The 10–15 μm Region

The 10–15 μm region is primarily associated with CH_{oop} bending vibrations, with bands falling in narrow subregions, characteristic of specific hydrogen adjacency classes (solo, duo, trio, etc., Hudgins & Allamandola 1999a; Hony et al. 2001; Bauschlicher et al. 2008, 2009). The 10–15 μm region of the computed spectra for the neutrals and for the ions is shown in Figure 6; a redshift of 15 cm^{-1} has been applied. The very compact PAHs studied in this work only have solo and duo hydrogens, except for $\text{C}_{24}\text{H}_{12}$ which has only duo hydrogens. The strongest band around 11 μm is a CH_{oop} produced by solo hydrogens and its intensity is very similar for all three charge states in agreement with previous work (Bauschlicher et al. 2008). For the neutrals, the solo band falls between 11.06 μm

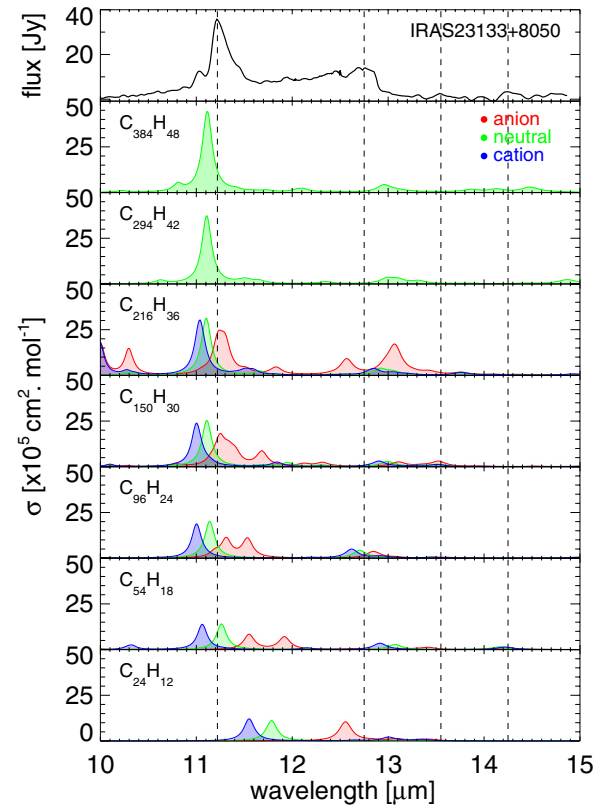


Figure 6. The 10–15 μm region of the spectra for the species studied in this work. A redshift of 15 cm^{-1} is used. For comparison, the top panel shows the observed spectrum of the prototypical class A source, IRAS 23133+8050, over the same wavelength region (Peeters et al. 2002). Dashed lines have been added at the dominant peaks of the observed spectra, at 11.22, 12.75, 13.55, and 14.25 μm .

(A color version of this figure is available in the online journal.)

($\text{C}_{54}\text{H}_{18}$) and 10.93 μm ($\text{C}_{384}\text{H}_{48}$). As the PAH size increases, the solo CH_{oop} feature shifts to a shorter wavelength and its position is converged for $\text{C}_{150}\text{H}_{30}$. For the cations, the solo band falls at shorter wavelength than for the neutrals between 11.19 μm ($\text{C}_{54}\text{H}_{18}^+$) and 10.89 μm ($\text{C}_{150}\text{H}_{30}^+$). The peak position also shifts to shorter wavelength as the PAH size increases. For the anions, two peaks can be assigned to the CH_{oop} vibrations of solo hydrogens and they fall at longer wavelength than for the neutrals and cations. The two peaks fall at 11.70 and 11.36 μm for $\text{C}_{54}\text{H}_{18}^-$. The band at 11.36 μm arises from a vibration in which only the solo hydrogens move, “only solos,” whereas the band at 11.70 μm is mostly due to the motion of solos with some contributions from duos. As the PAH size increases, the two peaks shift to shorter wavelength and the gap between them decreases until both peaks coalesce for $\text{C}_{150}\text{H}_{30}^-$ to form a broad feature. For $\text{C}_{96}\text{H}_{24}$, the “only solos” band falls at 11.33 μm and the band with mixed character falls at 11.13 μm . Finally, for $\text{C}_{150}\text{H}_{30}^-$, the “only solos” band falls at 11.07 μm and has a distinct shoulder. An additional peak is also present at 11.48 μm that can be attributed to an in-plane mode. The duo CH_{oop} falls around 12.8 μm for the neutrals and the band position is fairly insensitive to PAH size. Upon charging, the duo peak shifts to slightly shorter wavelength. For the ions, most of the duo peaks have a mixed character with contributions from duo and solo CH_{oop} bending modes.

An inspection of the spectra also shows that, as the size of the PAH increases, the number of bands in this region increases. While it might initially appear that the splitting of the duo bands

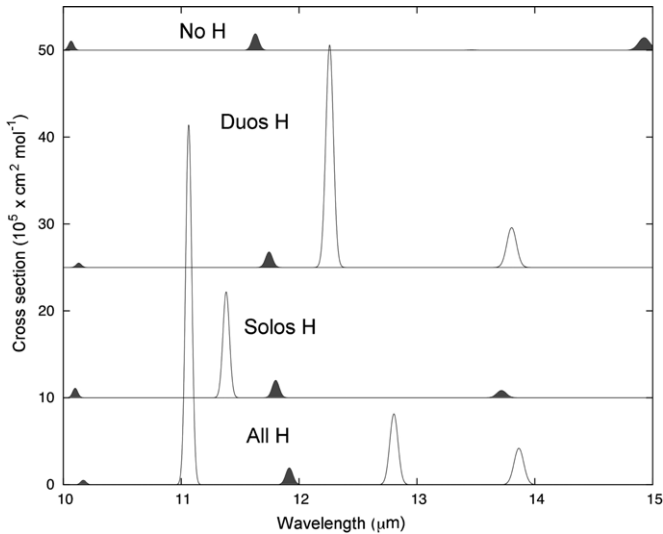


Figure 7. Influence of hydrogen mass on the 10–15 μm region for $\text{C}_{54}\text{H}_{18}$. “All H” is the normal spectra; “Solos H” means that the solo hydrogens have the normal hydrogen mass, while the mass of the duo hydrogens has been artificially reduced to 0.2 amu; “Duos H” means that the mass of solo hydrogens has been artificially reduced to 0.2 amu; and “No H” means that the mass of all hydrogens has been artificially reduced to 0.2 amu. The peaks corresponding to in-plane modes have been shaded in black. No redshift is used.

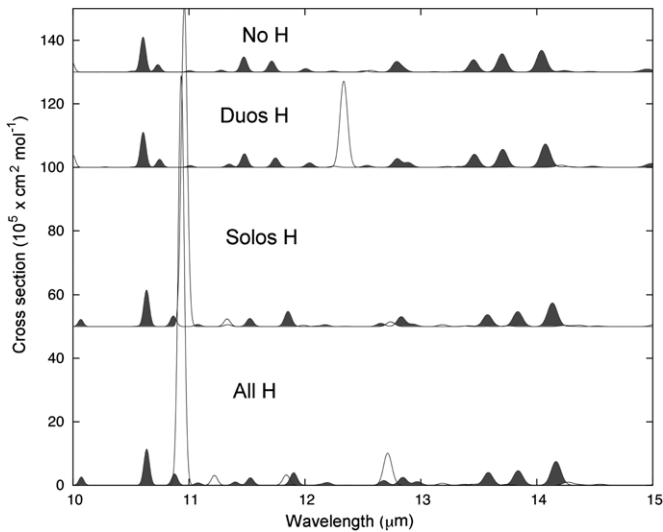


Figure 8. Influence of hydrogen mass on the 10–15 μm region for $\text{C}_{384}\text{H}_{48}$. The notation is the same as in Figure 7.

and the formation of mixed bands increase with PAH size, an inspection of the modes shows that an increasing number of in-plane modes appear in this region with increasing size. As noted previously (Bauschlicher et al. 2008, 2009) and described in the Appendix, additional insight into the modes in this region can be obtained by changing the mass of the hydrogen atoms. The in-plane modes in the decomposition of the spectra for $\text{C}_{54}\text{H}_{18}$ and $\text{C}_{384}\text{H}_{48}$ (shown in Figures 7 and 8) are shaded dark. The top plot in all of the figures is labeled “no H” and this indicates that the mass of all the hydrogens has been changed. Since the in-plane bands are relatively constant for all choices of hydrogen mass, they must arise from modes that do not have significant hydrogen involvement. For $\text{C}_{54}\text{H}_{18}$, only a few bands are present, whereas for $\text{C}_{384}\text{H}_{48}$, several bands have intensities comparable to the “coupled” duos. The presence of these in-plane bands complicates the interpretation of the spectra in terms of solo, duo, trio, etc., out-of-plane bends. We can conclude that

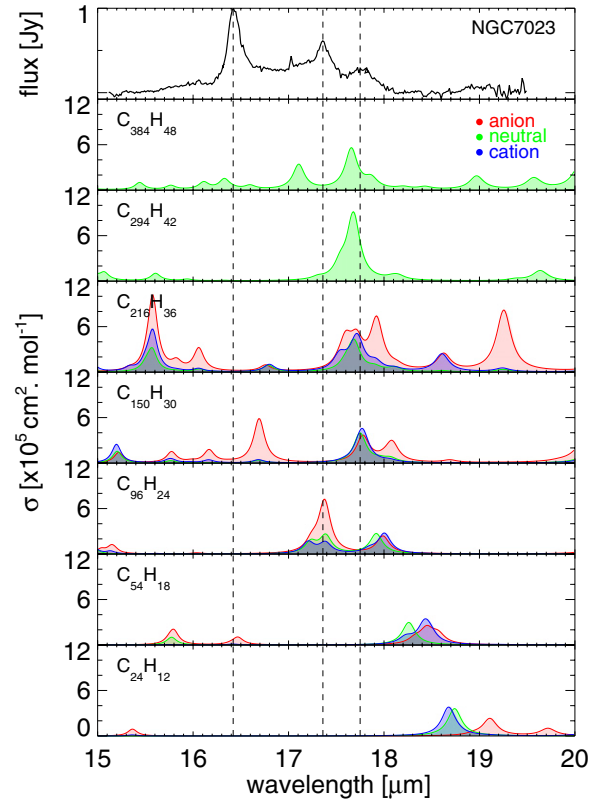


Figure 9. The 15–20 μm region of the spectra for the species studied in this work. A redshift of 15 cm^{-1} is used. For comparison, the top panel shows the observed spectrum of the reflection nebulae, NGC 7023, over the same wavelength region (Sellgren et al. 2007). Dashed lines have been added at the dominant peaks of the observed spectra, at 16.42, 17.36, and 17.75 μm .

(A color version of this figure is available in the online journal.)

as PAHs get larger in size, the spectra in the 10–15 μm region become more complex due to more and more in-plane features adding to the CH_{oop} bending modes.

3.2.4. The 15–20 μm Region

This region of the spectrum is the start of the transition from bands due to pure group molecular vibrations to bands due to involvement of larger parts of the PAH skeleton. The spectral characteristics in this region have previously been studied by Moutou et al. (1999), van Kerckhoven et al. (2000), Ricca et al. (2010), and Boersma et al. (2010) and have shown that shape and size are the main drivers of the spectral structure in the 15–20 μm region. Regular, compact PAHs have fairly simple spectra that show more bands with increasing PAH size. The feature that is common to all the spectra is an out-of-plane drumhead mode with $n - 1$; $n \geq 4$ circular nodes (which would be denoted $(0, n)$ for a classical drum). The value of n is dependent on PAH size as will be shown in the next section. As the PAH size increases, this mode shifts from 18.23 μm for $\text{C}_{24}\text{H}_{12}$, to 17.77 μm for $\text{C}_{54}\text{H}_{18}$, to 17.45 μm for $\text{C}_{96}\text{H}_{24}$, to 17.29 μm for $\text{C}_{150}\text{H}_{30}$, to 17.22 μm for $\text{C}_{216}\text{H}_{36}$, to 17.21 μm for $\text{C}_{294}\text{H}_{42}$, and to 17.20 μm for $\text{C}_{384}\text{H}_{48}$; see Figure 9 (n.b. the spectra have been redshifted by 15 cm^{-1}). Besides the out-of-plane mode, other bands are visible for PAHs with 96 carbons or more. For $\text{C}_{96}\text{H}_{24}$, a broad peak arises at 16.8 μm with one component at 16.95 μm due to in-plane C–H scissors and one component at 16.8 μm due to a mixed duo CH_{oop} bending mode that couples with an out-of-plane CC-skeletal bending mode. For $\text{C}_{150}\text{H}_{30}$,

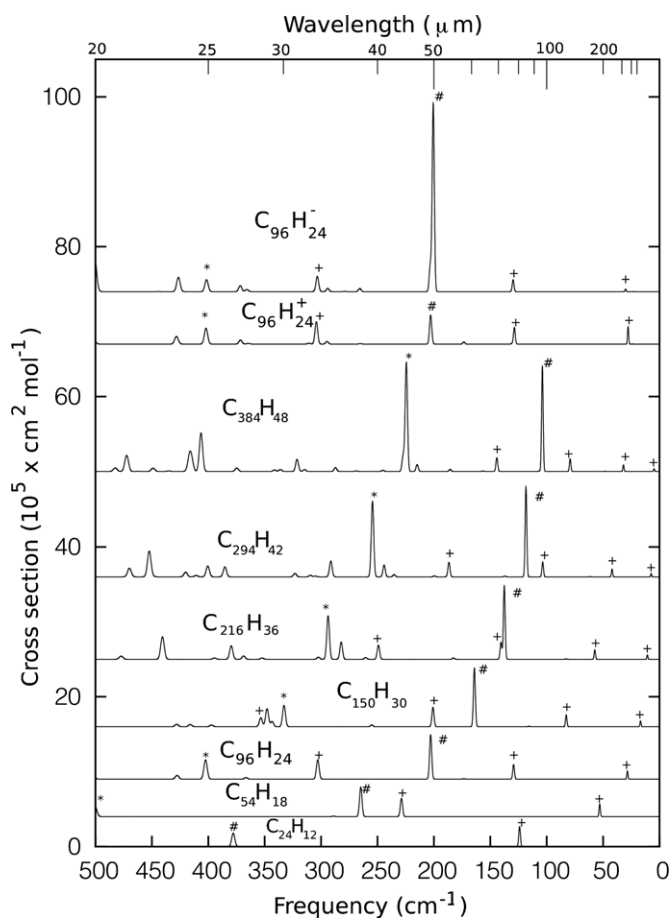


Figure 10. The 500–0 cm^{-1} region of the spectra for the neutrals studied in this work. The drumhead modes are marked with +, the jumping-jacks are marked with #, and the in-plane duo twists are marked with *. The spectra of $\text{C}_{96}\text{H}_{24}^-$ and $\text{C}_{96}\text{H}_{24}^+$ are also shown. No redshift is used.

a peak is also present at $19.60 \mu\text{m}$ which can be attributed to an in-plane elongation and compression mode. A band at $15.22 \mu\text{m}$ due to an in-plane elongation and compression mode and a band at $19.74 \mu\text{m}$ due to a combination of in-plane duo twisting and in-plane C–H scissors also appear for $\text{C}_{216}\text{H}_{36}$. Finally, for $\text{C}_{384}\text{H}_{48}$, two additional peaks with significant intensities are present: one at $16.68 \mu\text{m}$ due to in-plane C–H scissoring and one at $19.50 \mu\text{m}$ due to in-plane duo twist coupled with a skeletal elongation and compression.

3.2.5. The 20–3000 μm Region

This region of the spectrum, generally considered the far-infrared, is where bands are attributed to vibrations involving the molecular structure as a whole. This part of the PAH spectrum has bands that are typically an order of magnitude weaker than the mid-infrared bands (Mulas et al. 2005; Mattioda et al. 2009; Ricca et al. 2010; Boersma et al. 2011). The 20–3000 μm region of the spectra for the neutrals and for a representative ion studied in this work are shown in Figure 10. Three distinct classes of vibrational modes were identified which show distinct trends for both neutrals and ionized PAHs. For all three trends, the band positions shift to longer wavelengths as the PAH size increases. One class is denoted as “drumhead,” as the PAH molecular skeleton performs an out-of-plane motion like a drum. The lowest energy feature for each molecule can be described as the (0,1) out-of-plane drumhead mode of an ideal membrane.

The mode number (0,1) indicates that there is one circular node (the outside edge) but no nodes along the diameter. The (0,1) drumhead has the longest wavelength and the weakest features of the three series illustrated in these figures. The shorter wavelength drumhead bands for each molecule are those members of the drumhead series with additional circular nodes ((0, n), $n \geq 2$). In Figure 10, we show the trends for the (0,2), (0,3), and (0,4) members of the series. The intensities are weak and similar to those for (0,1). Ionization does not significantly affect the intensities of the drumheads, which are very weak.

The other two trends are due to in-plane modes denoted as “in-plane duo twist” and “jumping-jacks” and have stronger intensities than the drumhead modes (Figure 10). The “in-plane duo twist” has two pairs of duo hydrogens on two opposite corners twisting in the same direction (Figure 11(top left) shows one component of this mode). The duo hydrogens at the remaining four corners undergo some elongation and compression motion. This in-plane duo twist was not identified in previous work. One component of the degenerate “jumping-jacks” mode is shown in the top right of Figure 11. The in-plane duo twist mode extends from $12.47 \mu\text{m}$ for $\text{C}_{24}\text{H}_{12}$ to $44.56 \mu\text{m}$ for $\text{C}_{384}\text{H}_{48}$, while the jumping-jacks mode extends from $18.23 \mu\text{m}$ for $\text{C}_{24}\text{H}_{12}$ to $96.30 \mu\text{m}$ for $\text{C}_{384}\text{H}_{48}$.

The effect of adding or removing an electron on the peak positions and intensities is illustrated in Figure 10 for $\text{C}_{96}\text{H}_{24}$. We first note that ionizing the molecule splits these degenerate modes into two separate modes, but the splitting is small and, in general, one of the two bands carries virtually all of the intensity. As a result, the peak positions are unaffected by the change in charge, but the intensities of the “jumping-jacks” for the anions are significantly enhanced by about a factor of four. For the cations, there is a slight increase in the intensities, but the effect is much less dramatic.

Figure 11 shows that the lowest drumhead mode involves the out-of-plane motion of the whole carbon skeleton and of the hydrogen atoms at the PAH edge. As noted previously (Ricca et al. 2010; Boersma et al. 2011), the drumhead modes of compact PAHs behave like the drumheads of a free (not clamped) classical solid plate. Figure 12 shows a plot of the lowest drumhead frequency (in cm^{-1}) versus the inverse of the PAH area ($1/A$) for the three PAH families “coronene,” “ovalene,” and “pyrene.” The area, A , is taken as the surface delimited by the outer hydrogen atoms. In order to make predictions without having to compute the molecular structure, we derive a simple relation that is shown in the inset in Figure 12 that illustrates the three areas, A_1 , A_2 , and A_3 , that come into play when computing the total area A . A_1 is the area enclosed by the hexagonal carbon ring that is the PAH building block. A_2 is the area delimited by two C–H bonds on adjacent hexagonal rings and its value is $0.671 A_1$. A_3 is the area delimited by two adjacent C–H bonds on the same hexagonal skeleton and its value is $0.341 A_1$. The lowest drumhead modes for the three PAH families can be fitted using the same linear relation. The intensity of the (0,1) drumhead mode can also be fit to $1/A$ for the three PAH families; see Figure 12.

Figure 13 shows the frequencies (in cm^{-1}) of the in-plane duo twist and of the jumping-jacks versus the inverse of the number of hydrogen atoms N_{H} . As the PAH size increases, the PAH skeleton becomes easier to twist in the molecular plane and the in-plane modes shift to smaller wavenumber. The fitting for both modes is excellent. Unlike the drumhead modes where both the band position and intensity scale with $1/A$, the intensities of the duo twist and jumping-jacks scale differently from their

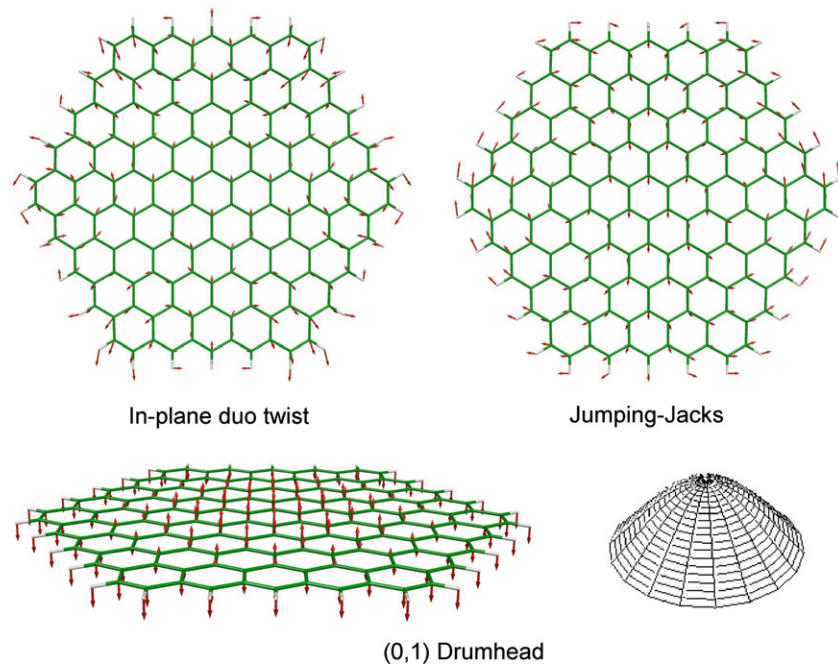


Figure 11. Illustration of the motion associated with the in-plane duo twist (top left), in-plane “jumping-jacks” (top right), and the out-of-plane (0,1) “drumhead” (bottom) modes. Note that the in-plane duo twist and jumping-jacks are degenerate modes and only one component is shown here. (A color version of this figure is available in the online journal.)

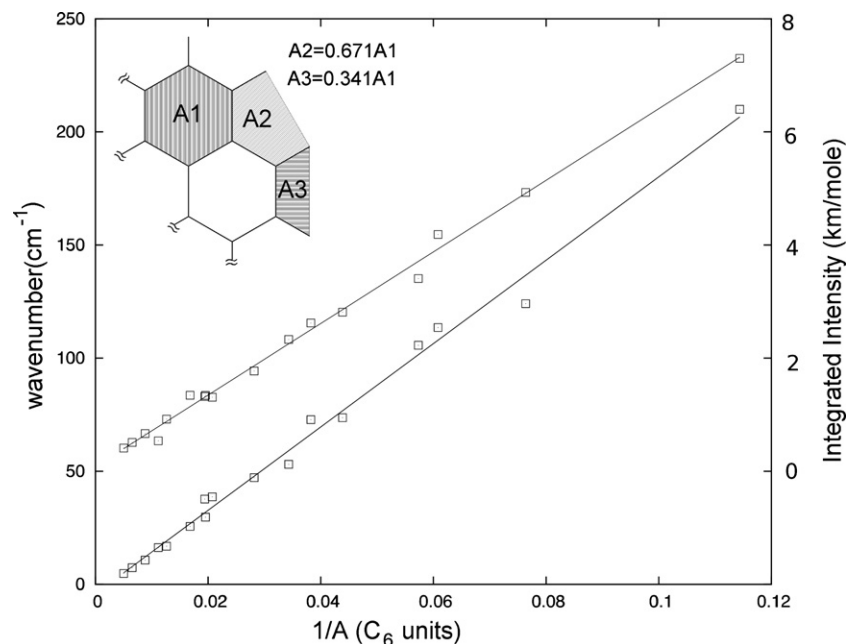


Figure 12. The lower line is the position of the (0,1) drumhead mode vs. the inverse of the area of the PAH ($1/A$), while the upper line is the intensity of the (0,1) drumhead mode vs. the inverse of the area of the PAH ($1/A$). The area includes the hydrogen atoms, as well as the carbon framework, as defined in the insert. The coronene, ovalene, and pyrene families are included in the plot.

positions, namely, the intensity of the duo twist scales with the square of the number of hydrogens while the intensity of the jumping-jacks scales with the number of hydrogens.

4. ASTRONOMICAL IMPLICATIONS

The spectroscopy of the PAHs in the coronene family has been presented in great detail in Section 3. Here, we compare and contrast these calculated spectra with the observations of the interstellar infrared emission bands. In our analysis,

we will also include the results for the compact coronene, ovalene, anthracene, tetracene, and VLPAAHSI families, and for the irregular VLPAAHSII. The results for the compact VLPAAHSI were presented by Bauschlicher et al. (2008), while those for the VLPAAHSII by Bauschlicher et al. (2009). In Section 4.1, we focus on spectroscopic aspects. Sections 4.2 and 4.3 discuss the astronomical implications of the calculated dependence of the integrated strength of the different bands on size within the different families. In Section 4.4, we compare model intensities of the different families with observed intensity ratios of the

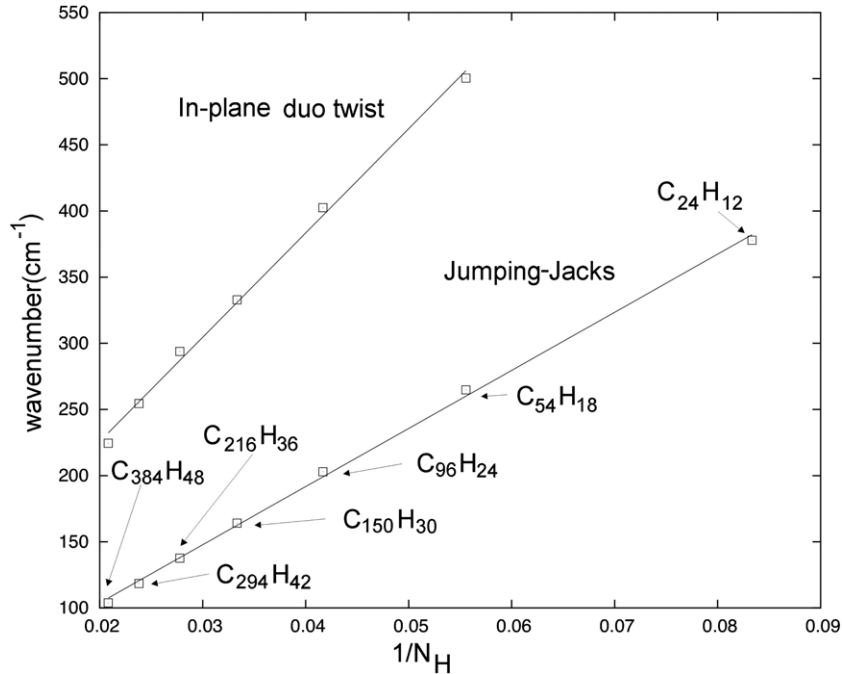


Figure 13. Position of the in-plane modes vs. the inverse of the number of H atoms.

infrared emission bands. Finally, in Section 4.5, the observed infrared emission bands observed toward the prototypical source IRAS 23133+6050 (Peeters et al. 2002) are fitted by the spectra of the different families.

4.1. Astronomical Band Positions

In this comparison, we have adopted a redshift of 15 cm^{-1} due to anharmonicity of highly vibrationally excited PAHs for each band. While the presence of such a redshift is well established by laboratory studies and the adopted value is in line with available data (Barker et al. 1987; Joblin et al. 1995; Pech et al. 2002; Oomens et al. 2003), we emphasize that this redshift may well be somewhat molecule and mode specific. In the comparison, we represent the theoretical spectra by Lorentzian profiles with the calculated integrated strength and variable widths as described in Section 2. This is only an approximation since the actual emission profile from a highly excited molecule will be redshifted, reflecting the anharmonicity of the interaction potential (Barker et al. 1987; Schlemmer et al. 1994; Joblin et al. 1995). Since the profile is a function of the excitation and molecular parameters and this dependence is not known for the molecules under consideration, we have refrained from a more complicated analysis. Further laboratory or theoretical studies will be required to assess these issues.

4.1.1. The 3.3 μm Band

The 3.3 μm feature is generally observed to be the strongest band in the 3 μm region of astronomical spectra (Figure 4). The profile of this band is very constant from source to source: very symmetric with a peak at $3.290 \mu\text{m}$ and a width of $0.040 \mu\text{m}$ (van Diedenhoven et al. 2004). The red rectangle, HD 44179, provides the best example of a source with a very different 3.3 μm band with a peak at $3.297 \mu\text{m}$ and an asymmetric (blueshaded) band with a width of $0.037 \mu\text{m}$ (Tokunaga et al. 1991; van Diedenhoven et al. 2004). Further studies of the 3.3 μm emission profile in the red rectangle have revealed that on the central position, the fea-

ture is very symmetric, with a width of $\simeq 0.035 \mu\text{m}$ and a peak at $3.298 \mu\text{m}$. With offset, a second component seems to grow in on the blue wing with a peak position at $3.28 \mu\text{m}$ and a very similar width (Song et al. 2007). It seems likely that these two components together make up the interstellar 3.3 μm feature in other sources in a ratio which is almost invariant.

Given the dependence of the intrinsic strength of the C–H modes on charge state (Langhoff 1996; Allamandola et al. 1999; Pauzat et al. 1997), the 3.3 μm band has been “universally” attributed to neutral PAHs. Later studies revealed that the intrinsic strength of the 3.3 μm band of large compact PAH cations is larger per C–H mode than for small PAH cations (Bauschlicher et al. 2008; Schmidt et al. 2009; Pauzat et al. 2010). However, most of the emission in the 3.3 μm feature can still safely be attributed to neutral PAHs (see Section 4.3). Given the limited heat capacity of PAH molecules, only small PAHs will contribute substantially to the emission at the shortest wavelengths and analysis of the observed 3.3/11.2 μm ratio—adopting a value for the intrinsic strength of the CH stretching and out-of-plane bending modes—implies sizes in the range of 50–100 C-atoms. We will revisit this issue in Section 4.2 on the basis of the calculations presented here.

Previously, the C–H stretching mode has been studied in compact PAHs and in irregular PAHs (Bauschlicher et al. 2008, 2009). These studies focused on the predominant C–H stretching mode of large, compact, neutral PAHs as the carrier of the interstellar 3.3 μm band, noting that the main C–H stretching band shifts to higher frequencies for irregular PAHs as a result of steric hindrance of bay hydrogens. Here, we emphasize that compact PAHs actually have two C–H stretching modes (cf. Figure 4). These two modes correspond to vibrations of solo and of duo C–H’s. Because of the symmetry, the intrinsic strength associated with the concerted motions of the corner H’s (duo modes) increases with size and these modes are still very comparable in strength to the solo modes even for very large PAHs. We suggest that the interstellar 3.3 μm band is due to a blending of the solo and duo modes in compact PAHs and that the invariant profile reflects a “fine-tuning” of the interstellar

PAH size distribution, limited on the small end by fragmentation of small PAHs and on the large end by the steep dependence on temperature—and therefore size—of emission at $3.3\ \mu\text{m}$. The variations in the profile of the $3.3\ \mu\text{m}$ band with distance in the red rectangle reflect then a shift in the size distribution of the emitting PAH family from large to small at large distances from the star. Such a shift may reflect the photoerosion of PAHs with time in the ejecta. The spatial behavior of the C_2 Swan bands in this source has also been interpreted in terms of the fragmentation of PAHs producing the parent molecule, C_2H_2 , which is quickly photolyzed to C_2 (Wehres et al. 2010). Alternatively, the second high-frequency band growing in with distance in the red rectangle may result from the increased importance of bay H's with distance, possibly again reflecting destruction of compact PAHs (Candian et al. 2012).

4.1.2. The 6.2, “7.7,” and $8.6\ \mu\text{m}$ Bands

Interstellar spectra in this wavelength range contain the strong 6.2, “7.7,” and $8.6\ \mu\text{m}$ bands (Figure 5) as well as a host of weaker bands (Peeters et al. 2002; Moutou et al. 1996). The astronomical $6.2\ \mu\text{m}$ band is typically redshaded and its peak position shifts by almost $0.1\ \mu\text{m}$ from source to source. The peak can occur as shortward as $6.2\ \mu\text{m}$ in some H II regions and reflection nebulae but has shifted to $6.3\ \mu\text{m}$ in sources dominated by circumstellar material. The observed variation in peak position of the astronomical $6.2\ \mu\text{m}$ band may reflect variable contributions of these two “end members” (Peeters et al. 2002). The astronomical “7.7” μm band generally has two components peaking at 7.6 and $7.8\ \mu\text{m}$. The relative contribution of these two modes varies from source to source, shifting the peak position of the astronomical band from 7.6 to $7.8\ \mu\text{m}$ (Peeters et al. 2002). In some sources with circumstellar material illuminated by a cool star, the peak position may shift all the way to $8.2\ \mu\text{m}$. The variations in the 6.2 and $7.7\ \mu\text{m}$ go hand in hand and a 6.2 (6.3) μm peak position generally goes with a strong 7.6 (7.8) μm component. The $8.6\ \mu\text{m}$ band is very symmetric and shifts only slightly ($<0.05\ \mu\text{m}$) from source to source. Weak bands have been detected at 6.0 , 7.0 , and $7.4\ \mu\text{m}$ (Moutou et al. 1996; Peeters et al. 2002). Due to a lack of high-quality spectra, spectral variations of these weak bands have gone unexplored.

In PAHs, the 6.2 and “7.7” μm bands are due to C–C stretching modes while the $8.6\ \mu\text{m}$ band is due to the CH_{ip} bending mode, albeit these modes in this wavelength range actually have a strong mixed character. The C–C modes are intrinsically very strong in cations and the 6.2 and “7.7” μm bands are therefore attributed to PAH cations (Hudgins & Allamandola 1999b; Peeters et al. 2002). Observed variations in the peak position and profile of the 6.2 and/or “7.7” μm bands have been attributed to the substitution of nitrogen in variable positions of the carbon skeleton (Peeters et al. 2002; Hudgins et al. 2005), to variable contributions by aliphatic hydrocarbons attached to the PAH skeleton (Sloan et al. 2007; Pino et al. 2008), and to closed shell cations such as protonated PAHs (Knorke et al. 2009; Ricca et al. 2011a). None of these explanations provide a simple explanation for the concerted variations of the 6.2 and “7.7” μm bands. The $8.6\ \mu\text{m}$ band has been attributed to emission by large compact PAHs (Bauschlicher et al. 2008). The C_{60} molecule may give a variable but minor contribution to the $8.6\ \mu\text{m}$ emission band and perhaps a more important contribution to the $7.0\ \mu\text{m}$ band (Sellgren et al. 2010; Cami et al. 2010). Here, we confirm the charge dependence of the intrinsic strength of the C–C modes for very large compact PAHs. In addition, we emphasize that the ratios of the intrinsic

strength of the main bands in this wavelength region are very sensitive to size and shape. Very large, compact PAHs show a broad and very intense distribution of bands between 6 and $7\ \mu\text{m}$ and a very strong $8.6\ \mu\text{m}$ band that is very much in contrast to the simplicity of the observed spectra. The former reflects the increased number of C–C modes. We expect that the inherent asymmetry of very large, irregular PAHs will have even more infrared activity induced in this wavelength region. Perusal of our spectra suggests that compact PAHs with sizes larger than 150 C-atoms make a minor contribution to the observed interstellar spectra, if present at all, and this is likely an upper limit to all PAHs (compact or irregular).

4.1.3. The C–H Out-of-plane Modes

Interstellar spectra show two strong bands, at 11.2 and $12.7\ \mu\text{m}$ (Figure 6), with variable relative strength (Hony et al. 2001). The $11.2\ \mu\text{m}$ band is redshaded while the $12.7\ \mu\text{m}$ band is blueshaded. Only very small variations in the profiles of these bands have been observed (van Diedenhoven et al. 2004). The strength of the $11.2\ \mu\text{m}$ band is strongly correlated with the $3.3\ \mu\text{m}$ C–H stretching mode in interstellar spectra and varies strongly with respect to the strength of the 6.2 and “7.7” μm C–C modes (Hony et al. 2001). In contrast, the observed strength of the $12.7\ \mu\text{m}$ band correlates with the 6.2 and “7.7” μm C–C modes and varies strongly with respect to the $11.2\ \mu\text{m}$ band. In addition, there are weak bands at 11.0 , 12.0 , 13.5 , and $14.2\ \mu\text{m}$. Of these, only the $11.0\ \mu\text{m}$ band has been investigated in detail and its strength also correlates with the C–C modes rather than the $11.2\ \mu\text{m}$ band (Rosenberg et al. 2011). There is also an indication that the 12.0 and $13.5\ \mu\text{m}$ bands split into two components where the high-frequency component correlates with the C–C modes (Rosenberg et al. 2011).

This wavelength range is characteristic for the CH_{oop} bending modes of PAHs. Spectroscopic studies have shown that the $11.2\ \mu\text{m}$ band is due to solo CH_{oop} modes in PAHs while the $12.7\ \mu\text{m}$ band can be attributed to duo and/or trio CH modes. As for the $3.3\ \mu\text{m}$ CH_{str} mode, the CH_{oop} modes are very strong in neutral PAHs and weak in PAH cations (relative to the C–C modes; Langhoff 1996; Allamandola et al. 1999; Pauzat et al. 1997) and the $11.2\ \mu\text{m}$ band is therefore widely considered to be arising from neutral PAHs (Hony et al. 2001; Szczepanski & Vala 1993a, 1993b).

In this framework, the good correlation of the strong neutral $12.7\ \mu\text{m}$ CH_{oop} mode with the cation C–C modes is somewhat curious. Honny et al. (2001) was forced to conclude that the band correlation reflects a correlation of molecular structure and charge state with environment. That is, those environments which favor large PAHs and the $11.2\ \mu\text{m}$ band also favor neutral PAHs, while in regions where open uneven molecular structures and the $12.7\ \mu\text{m}$ band dominate, PAHs are predominantly charged. The high far-ultraviolet fluxes that lead to high abundances of PAH cations also photolyze PAHs, and the loss of (peripheral) C-atoms then leads to the formation of more “corners” and thus a stronger $12.7\ \mu\text{m}$ band. The solo CH_{oop} mode shifts to higher frequencies in PAH cations and these species have been proposed as the carriers of the weak interstellar $11.0\ \mu\text{m}$ band (Rosenberg et al. 2011). The 13.5 and $14.2\ \mu\text{m}$ bands have been attributed to trio and quartet modes in neutral PAHs (Hony et al. 2001).

Because of the intrinsic structure of the molecules investigated, the results presented here pertain to solo and duo modes. Our study confirms the earlier results that the solo mode is strong in neutral species and weak in cations relative to the C–C modes.

With increasing size, the solo CH_{oop} mode shifts to higher frequencies and for $N_{\text{C}} > 96$ is very stable in peak position in the coronene family (cf. Figure 6), and this holds for the ovalene family as well. The CH_{oop} modes are slightly shifted to higher frequencies for cations with respect to the neutral position and show the same trend with increasing size. The duo modes occur near $12.8 \mu\text{m}$ (cf. Figure 6).

4.1.4. The C-skeletal Modes

Astronomical observations show very simple spectra in this wavelength range (Figure 9), with main bands at 16.4 and $17.4 \mu\text{m}$ and weaker features at 15.8 , 17.0 (broad), and $17.8 \mu\text{m}$ (Werner et al. 2004; Smith et al. 2007; Sellgren et al. 2007; Boersma et al. 2010). Earlier *ISO-SWS* studies revealed a broad plateau of emission in this wavelength region which is likely due to a blending of these bands in the large aperture of these observations (van Kerckhoven et al. 2000). In some sources, a broad plateau appears even within the much smaller *Spitzer-IRS* aperture (Boersma et al. 2010). The overall emission complex in this wavelength range correlates well with the strength of the $11.2 \mu\text{m}$ band (Smith et al. 2007). However, the individual components in this wavelength range do not correlate well with each other or with shorter wavelength bands except for the $16.4 \mu\text{m}$ band, which seems to correlate with the $6.2 \mu\text{m}$ band (Smith et al. 2007). Finally, there is a band at $18.9 \mu\text{m}$ which shows a distinctly different spatial behavior than the other bands (Sellgren et al. 2010). The $17.4 \mu\text{m}$ band has two components, of which one correlates spatially with the $18.9 \mu\text{m}$ (Sellgren et al. 2010).

Bands in this wavelength region are due to C–C deformation modes. Calculations reveal very complex spectra, generally with many bands that are characteristic for individual species and this has led to the conclusion that a few PAHs dominate the interstellar PAH family (Boersma et al. 2010). No specific molecular identifications have been made except for the $16.4 \mu\text{m}$ band, which has been attributed to the breathing mode in pendent rings or in PAHs with “pointy” edges (Moutou et al. 2000; van Kerckhoven et al. 2000; Ricca et al. 2010; Boersma et al. 2010). These previous studies focused on comparison to the whole database and therefore on non-symmetric PAHs. Spectra are much simpler in this wavelength range for the very symmetric, compact PAHs in the coronene (and ovalene) families presented here with typically one dominant mode (Figure 9). These bands are due to high-order drumhead modes (e.g., $(0, n)$ with n large) where the corners act as nodes; the so-called crumpling mode or crash dummy mode. The band at $18.6 \mu\text{m}$ in $\text{C}_{24}\text{H}_{12}$ shifts to higher frequency with increasing PAH size and seems to converge to a position near $17.8 \mu\text{m}$ in the calculations. However, there is no obvious identification for the interstellar $17.4 \mu\text{m}$ band in the calculated spectra of the coronene family and, of course, this family does not show the $16.4 \mu\text{m}$ breathing mode. Hence, while the simplicity of the observed spectra point toward the dominance of compact PAHs in the interstellar PAH family, the coronene and ovalene families do not seem to be the predominant carriers. Following Cami et al. (2010), the $18.9 \mu\text{m}$ band and the correlated $17.4 \mu\text{m}$ component in the interstellar spectra are generally attributed to emission by the neutral fullerene, C_{60} .

4.1.5. The Far-infrared

No PAH-related bands have been observed in this wavelength region, yet. However, the opening up of this window by *Herschel-PACS* and future *SOFIA* instruments may well reveal new bands. Previous theoretical studies have revealed that large

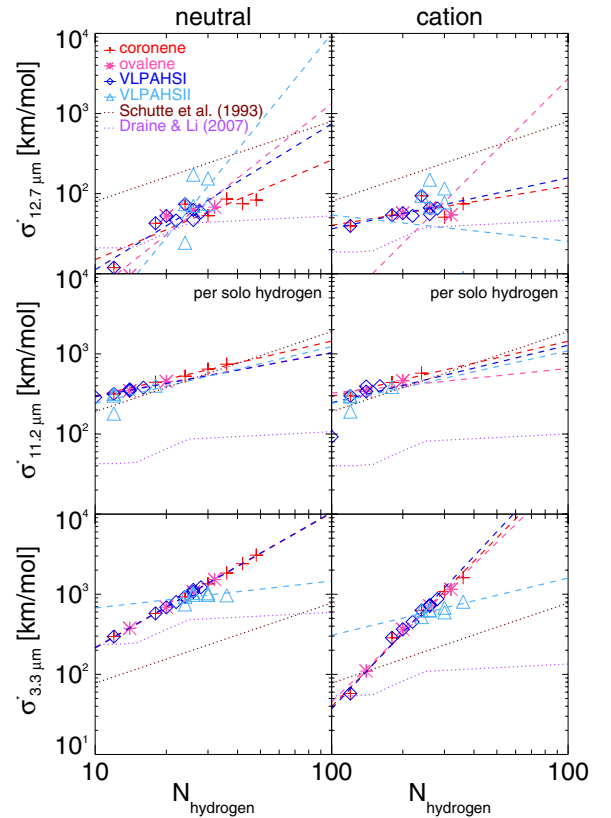


Figure 14. Intrinsic strength of the C–H modes at 3.3, 11.2, and $12.7 \mu\text{m}$ as a function of the number of hydrogen atoms. The power-law functions fitted to the data are presented in Table 2. For comparison, the relations used by Schutte et al. (1993) and Draine & Li (2007) in their generic PAH emission models are also shown.

(A color version of this figure is available in the online journal.)

PAHs show rich spectra at long wavelengths (Ricca et al. 2010; Boersma et al. 2011). The richness of the spectra increases with PAH size and for irregular PAHs. The results presented here show that for compact PAHs, the spectra show regular behavior. Besides the lowest vibrational mode, the drumhead mode in which the whole PAH vibrates out of plane, we also recognize “jumping-jack” and in-plane duo twist modes in the calculated spectra. All three bands shift toward longer wavelengths with increasing size but the latter two show pile-up behavior in their peak frequency (near 220 and 100 cm^{-1}). Hence, they would be excellent candidates for future searches of PAH bands in this wavelength range. The drumhead mode is much weaker and does not show this behavior. So, while this band would be very “telling” in terms of PAH size (actually area), it is a less favorable band to be searched for unless a “single” PAH dominates the interstellar PAH family. The regular behavior of the calculated spectra (see Figures 12 and 13) will facilitate the interpretation of these bands if they were to be detected.

4.2. Intrinsic Strength

The calculated intrinsic strength of the C–H and C–C modes for neutral and cationic PAHs are shown in Figures 14 and 15 as a function of the number of H or C atoms in the species. For a number of small PAHs, the calculated strength of these modes has been compared to matrix studies and shown to agree well, except for the neutral C–H stretching mode which is calculated to be a factor two stronger than measured (Langhoff 1996). Sometimes, this has led to a general, downward scaling in the

Table 2
Power-law Functions for the Intensities of the C–H and C–C Modes (see Figures 14 and 15)

C–H Modes								
Band	Coronene		Ovalene		VLPAAHSI		VLPAAHSII	
	Neutral $I(N_H)$	Cation $I(N_H)$	Neutral $I(N_H)$	Cation $I(N_H)$	Neutral $I(N_H)$	Cation $I(N_H)$	Neutral $I(N_H)$	Cation $I(N_H)$
3.3	$4.5 \times N_H^{1.7}$	$0.039 \times N_H^{3.0}$	$4.3 \times N_H^{1.7}$	$0.065 \times N_H^{2.8}$	$4.4 \times N_H^{1.7}$	$0.025 \times N_H^{3.2}$	$310 \times N_H^{0.34}$	$59 \times N_H^{0.71}$
11.2	$62 \times N_H^{0.68}$	$61 \times N_H^{0.69}$	$87 \times N_H^{0.54}$	$160 \times N_H^{0.31}$	$83 \times N_H^{0.55}$	$47 \times N_H^{0.71}$	$47 \times N_H^{0.71}$	$53 \times N_H^{0.86}$
12.7	$0.86 \times N_H^{1.2}$	$13 \times N_H^{0.49}$	$0.027 \times N_H^{2.3}$	$0.0036 \times N_H^{2.9}$	$0.17 \times N_H^{1.8}$	$8.4 \times N_H^{0.64}$	$0.000053 \times N_H^{3.6}$	$120 \times N_H^{-0.33}$
C–C Modes								
Band	Coronene		Ovalene		VLPAAHSI		VLPAAHSII	
	Neutral $I(N_C)$	Cation $I(N_C)$	Neutral $I(N_C)$	Cation $I(N_C)$	Neutral $I(N_C)$	Cation $I(N_C)$	Neutral $I(N_C)$	Cation $I(N_C)$
6.2	$0.19 \times N_C^{1.5}$	$7.5 \times N_C^{1.3}$	$0.24 \times N_C^{1.5}$	$8.7 \times N_C^{1.1}$	$0.26 \times N_C^{1.5}$	$17 \times N_C^{1.0}$	$1.5e^{-5} \times N_C^{3.6}$	$18 \times N_C^{1.1}$
7.7	$4.4 \times N_C^{0.67}$	$0.019 \times N_C^{2.4}$	$2.3 \times N_C^{0.70}$	$4.0 \times N_C^{1.3}$	$19 \times N_C^{0.3}$	$0.017 \times N_C^{2.5}$	$2.0e^{-5} \times N_C^{3.3}$	$0.005 \times N_C^{2.7}$
8.6	$0.28 \times N_C^{1.2}$	$0.38 \times N_C^{1.7}$	$1.5 \times N_C^{0.89}$	$13 \times N_C^{0.83}$	$0.35 \times N_C^{1.2}$	$0.67 \times N_C^{1.5}$	$2.8e^3 \times N_C^{-0.75}$	$0.082 \times N_C^{2.1}$

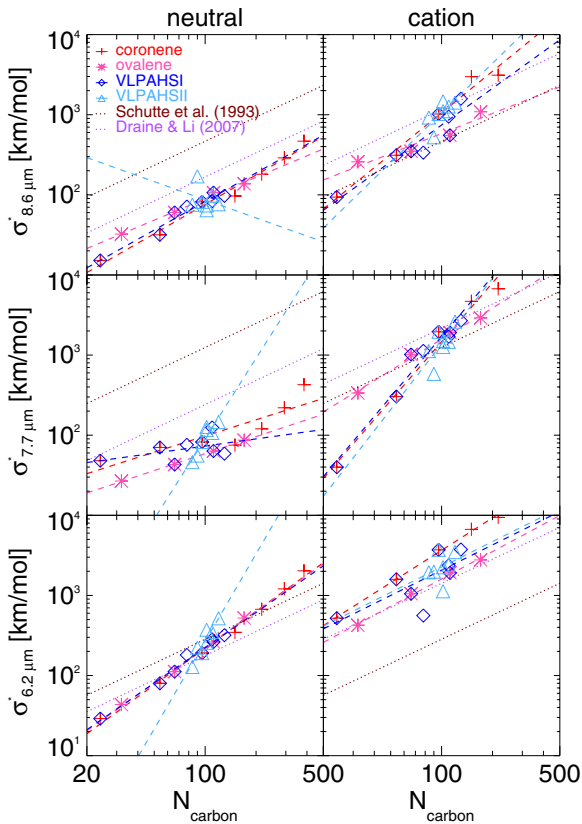


Figure 15. Intrinsic strength of the C–C modes at 6.2, 7.7, and 8.6 μm as a function of the number of carbon atoms. The power laws fitted to the data are presented in Table 2. For comparison, the relations used by Schutte et al. (1993) and Draine & Li (2007) in their generic PAH emission models are also shown. (A color version of this figure is available in the online journal.)

strength of this mode but we have refrained from doing so here, since the general applicability of this scaling factor for large PAHs has not been validated. Excluding the very irregular PAHs, denoted VLPAAHSII (Bauschlicher et al. 2009), the calculations reveal a very regular intrinsic strength-size relation for the coronene and ovalene families and for the regular VLPAAHSI (Bauschlicher et al. 2008; Figures 14 and 15 and Table 2), which will facilitate modeling of the observations in terms of

families of interstellar PAHs. However, we emphasize that the calculated relationships are not linear in N_C or N_H . It should be kept in mind that the intrinsic strength of vibrational modes is proportional to the derivative of the dipole moment associated with the vibration. With increasing size, the “leverage arm” of the vibration generally increases and the dependence on size is therefore steeper. The calculated relationships are thus somewhat different from those employed in models (Schutte et al. 1993; Draine & Li 2007). In some sense, this is a second-order effect since only the relative strength of the various modes enters in the emission models and variations in the behavior of the different modes are more limited. Nevertheless, there are noticeable differences and this has to be included in future model studies.

The behavior of the 3.3/11.2 μm bands is of particular interest since this has often been used as a size indicator of the emitting interstellar PAHs. Figure 16 shows the ratio of the emission in the 3.3 μm CH_{str} mode to the solo CH_{oop} mode as a function of the size of the PAH calculated for the coronene and ovalene families. The calculations take the individual characteristics of the molecule (heat capacity, temperature cascade, intrinsic strength of the modes) fully into account (Boersma et al. 2010; Bauschlicher et al. 2010). The simple relationship obvious in these calculations illustrates the power of this method for determining the size range relevant for the interstellar PAH family. Comparison to the observed range in this ratio implies that the “average” size of the emitting PAH families varies between 70 and 140 C-atoms from source to source. This is somewhat smaller than the sizes derived if the Draine & Li (2007) relationships are employed. We note (again) that the intrinsic strength of the C–H stretching mode has not been reduced by the factor two indicated by a comparison between theory and experiments for small PAHs. Such a reduction would reduce the sizes in the interstellar PAH family to the range 40–100 C-atoms. This latter range is in good agreement with the earlier estimates on PAH sizes (Allamandola et al. 1985; Schutte et al. 1993) that were based upon experimental studies of small PAHs.

4.3. Emergent Intensities

The observed spectra are often interpreted in terms of neutral and cationic bands (Hony et al. 2001; Rapacioli et al. 2005; Berné et al. 2007). Here, we reinvestigate this conclusion in

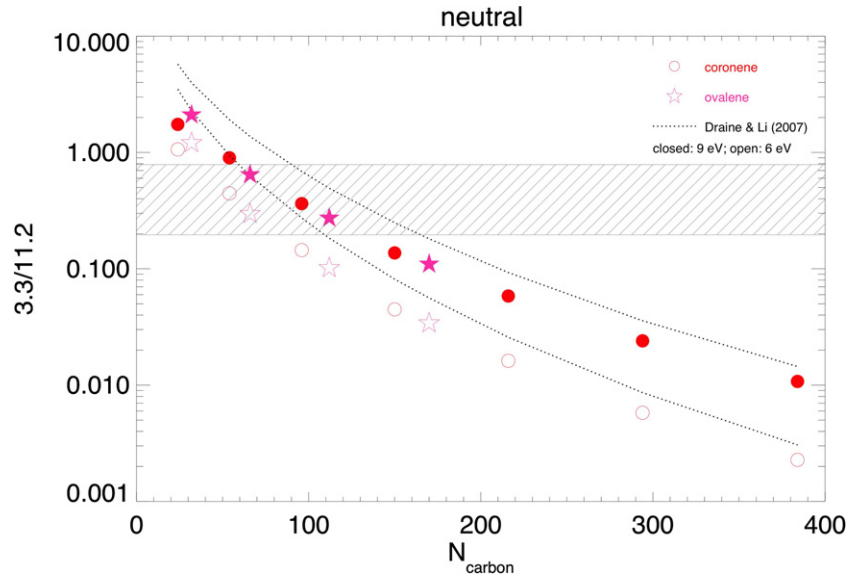


Figure 16. Strength of the 3.3/11.2 μm ratio as a function of the number of carbon atoms for the coronene and ovalene families at two excitation levels: 6 and 9 eV. The dotted lines show the results when using the generic relationship used by Draine & Li (2007). The shaded region indicates the observed astronomical range. (A color version of this figure is available in the online journal.)

view of the complicated behavior with size of the intrinsic strength of the different modes. We have modeled the interstellar emission spectra for PAHs in the coronene and ovalene families, taking the individual emission properties of the molecules fully into account (Boersma et al. 2010; Bauschlicher et al. 2010). Besides the vibrational characteristics calculated in this paper, the emission spectra will also depend on the amount of energy (initially) absorbed by the emitting species, which depends on the characteristics of the UV and visible radiation field as well as the absorption properties of the PAH. The latter are weakly dependent on the size and the charge state of the PAH under consideration. We have evaluated the mean absorbed energy and its dispersion for different radiation fields. The UV and visible absorption properties are not known for the specific PAHs considered here. Small neutral PAHs will only absorb in the near UV but as the size increases the first absorption system will shift into the visible (Clar 1972; Platt 1956). This narrowing of the band gap has been well studied experimentally for hydrocarbon solids (Robertson 2002), and the more scanty experimental and theoretical data on PAHs are in good agreement with this expectation (cf. Schutte et al. 1993; Mallocci et al. 2011). Here, we have adopted the generic absorption properties derived from these studies for neutral PAHs as a function of size by Draine & Li (2007). Because of the presence of unfilled valence states, even small, ionized PAHs will show visible absorption (Mallocci et al. 2011; Shida & Iwata 1973). Here, we have adopted the PAH absorption properties measured by Mattioda et al. (2005), which show (weak) absorption well into the near-IR. We have considered incident radiation fields which are appropriate for the photodissociation regions (PDRs) associated with H II regions (e.g., an O6 star with $T_{\text{eff}} = 38,000$ K) and a reflection nebula (e.g., a B2 star with $T_{\text{eff}} = 20,000$ K).

The results show that the mean excitation energy is mainly sensitive to the characteristics of the stellar radiation field with mean energies ranging from $\simeq 6$ to $\simeq 9$ eV and dispersions from 2 to 3 eV for B2 to O6 stars. This variation in the mean absorbed energy reflects the much hotter energy distribution of an O versus a B star. In contrast, size or charge has very little influence on the mean energy of the absorbed photon. For these types

of stars, the strong UV radiation field dominates the photon absorption process and absorption then occurs in the $\pi \rightarrow \pi^*$ system around 2200 Å and all PAHs “look alike.” Consequently, for sufficiently hard UV fields such as these, the average energy deposited in each PAH is completely insensitive to PAH size. The molecular specific absorption properties of individual PAHs (e.g., dependence on size or charge state) are limited to the visible and near-IR spectral domain, where we should emphasize that the visible absorption system in large neutral or ionized PAHs is very weak (typically only 0.01 that in the UV) and is therefore of less importance. Conversely, PAH size or charge effects on the mean absorbed photon energy will only show up in regions illuminated by fairly cool stars, but very little data exist for stars cooler than 8000 K. The interstellar radiation field contains two components; besides the UV component dominated by early B stars, there is much stronger visible and near-IR component resulting from cooler stars. The relative importance of PAH vibrational excitation by visible and near-IR photons versus that by UV is discussed in detail by Mattioda et al. (2005). In general, while visible and near-IR photons can pump an important fraction of the PAH IR emission from some cool stars, the PAH absorption process is generally dominated by the UV component—basically reflecting the high-UV absorption cross section of PAHs—with a mean absorbed photon energy of 6 eV and little dependence on size or charge state. The dispersion is now slightly larger, reflecting the small but finite probability to absorb a visible photon. Figure 17 illustrates that the most extreme variations that might be expected are less than 10%, and hence we feel justified in assessing the astronomical implications of the DFT calculations by comparison with astronomical model calculations at the average absorbed photon energy. Therefore, in our analysis of the PAH emission characteristics, we will adopt mean absorbed photon energies of 6 and 9 eV as representative of most of the bright PAH emission zones. Finally, important individual aspects of the excitation process such as the energy lost to photoionization and photodehydrogenation, or energy gained by PAH cation–electron recombination and hydrogenation are not taken into account.

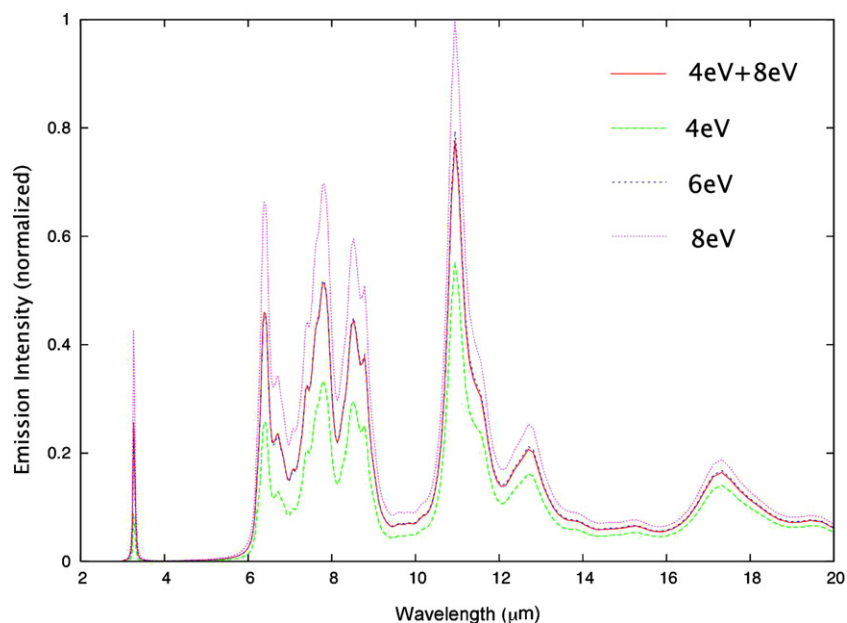


Figure 17. Average emission spectra of all of the coronene species studied (that is, all structures and all charge states) for absorbed photon energies of 4, 6, and 8 eV. The curves have been normalized to the maximum intensity for the 8 eV spectra. The average of the 4+8 eV spectra is also given and is so similar to the 6 eV spectra that it is difficult to separate the lines; i.e., the red and blue lines are hard to distinguish.

(A color version of this figure is available in the online journal.)

Figure 18 shows the calculated cumulative emission intensity as a function of wavelength for neutral and cationic species in the coronene and ovalene families plus the compact VLPAHI and irregular VLPAHII. It appears that all families show the same trends. For small neutral PAHs, a large fraction (up to 0.5) of the absorbed energy is emitted in the $3.3 \mu\text{m}$ CH_{str} mode and very little is contributed by the C–C modes (≈ 0.1) between 5 and $10 \mu\text{m}$. The remainder is mainly emitted in the CH_{oop} modes ($10\text{--}15 \mu\text{m}$) with a very small contribution (≈ 0.05) by the skeletal modes at long wavelengths. With increasing size, the balance in the emission intensity shifts from the CH_{str} mode toward the CH_{oop} modes. For very large PAHs ($N_{\text{C}} > 100$), some 0.3 of the emission intensity may be emitted in the C–C modes while longer wavelength modes may take up 0.2. For the cations, the results are very simple: some 0.7–0.8 comes out in the C–C modes and the remainder is roughly equally divided between CH_{oop} and longer wavelength skeletal modes (Figure 18). The emission in the CH_{str} mode is always negligible. Hence, we conclude that the calculations presented here support ascribing the C–H modes largely due to neutral PAHs while the C–C modes are cationic in character.

4.4. Comparison to Observations

4.4.1. C–H Modes

As discussed above (Sections 4.1.3, 3.2.4, and 4.2), the C–H modes are very characteristic for the size and molecular edge structure of the emitting species in the interstellar PAH family. Figure 19 compares the calculated intensity ratio of the $3.3/11.2 \mu\text{m}$ bands and the $12.7/11.2 \mu\text{m}$ bands for the different PAH families considered with the observations. While the calculated values for the $3.3/11.2 \mu\text{m}$ bands agree well with the observations when PAHs in the proper size range are considered (see Section 4.2), the $12.7/11.2 \mu\text{m}$ value falls very much at the low end of the observed ratio (Figure 19). It is clear that the coronene and ovalene families—each with only six corners in their structures—do not have the proper solo-to-duo-and-trio

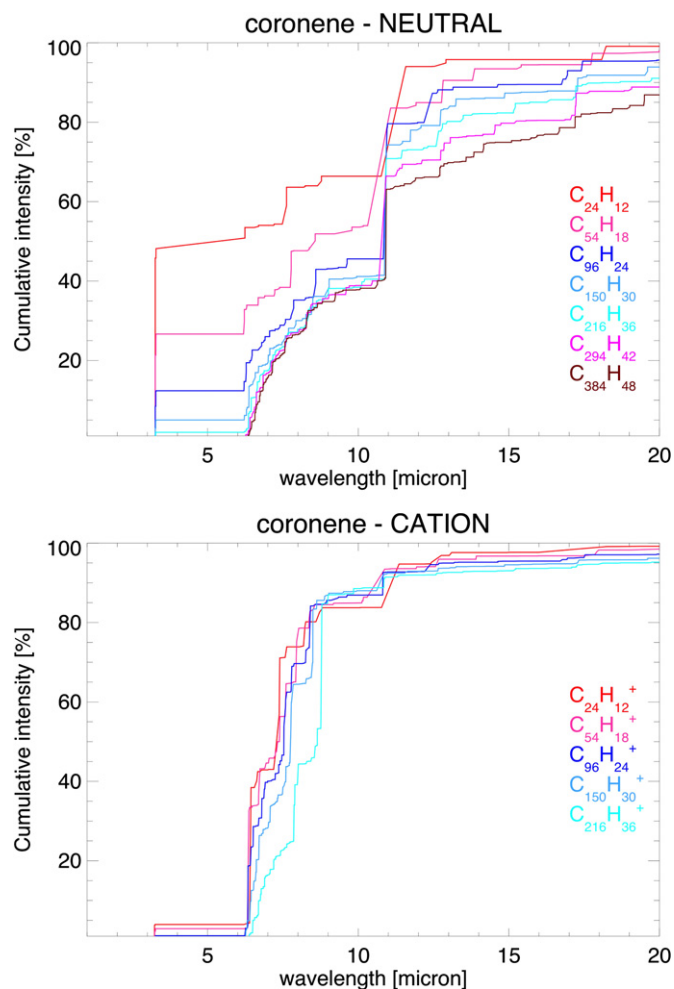


Figure 18. Cumulative intensity as a function of wavelength for the members of the coronene family, for both neutrals and cations at an excitation level of 9 eV. (A color version of this figure is available in the online journal.)

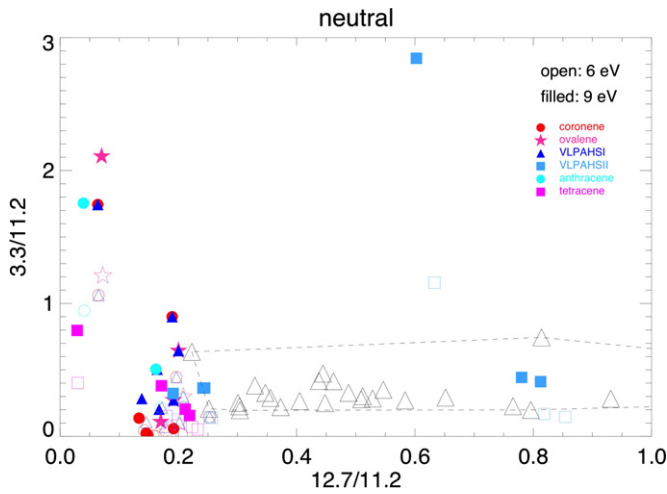


Figure 19. Strength of the 3.3/11.2 vs. 12.7/11.2 μm band strength ratio at two levels of excitation: 6 and 9 eV. The large triangles show the observations, outlined by the dashed outline.

(A color version of this figure is available in the online journal.)

modes. The species that dominate the interstellar PAH family must have a more irregular edge structure than these two families possess. Indeed, the very irregular PAHs with N_C equal to 84, 102, and 110 (Bauschlicher et al. 2009) do a good job in explaining the most extreme 12.7/11.2 μm values observed. Perhaps the zig-zag edges of PAHs are more favored in interstellar space than the armchair structure of the compact PAHs considered here (Berné & Tielens 2011).

4.4.2. C–C Modes

As discussed in Section 4.1.2, the strength of the bands in the 5–10 μm range is very sensitive to the PAH size. In Figure 20, we compare the calculated strength of the 7.7/6.2 versus the 8.6/6.2 μm bands with the observations (Peeters et al. 2002). In this comparison, we have included the PAHs in the coronene, ovalene, anthracene, and tetracene families as well as the very large irregular PAHs calculated by Bauschlicher et al. (2009). The calculations reveal a very large range in 7.7/6.2 and 8.6/6.2 μm ratios. This range is much larger than observed, indicating that only a small size range of PAHs contribute to the observed interstellar emission spectra. While the calculations cover both the range in the observed 7.7/6.2 ratio and in the 8.6/6.2 μm ratio, they do not do so at the same time. We notice an indication of a trend with the underlying structure of the PAH family. The coronene family (“circles” of hexagons surrounding a single benzene ring) are further displaced from the observed range than the ovalene family (“circles” of hexagons surrounding a two fused benzene rings). PAH families consisting of “circles” of hexagons surrounding larger fused ring structure seems to approach the data even more. So, while symmetrically centered, compact PAH families seem to be key to the interstellar PAHs, somewhat different central building blocks may be indicated.

4.4.3. The CH_{oop} Modes in Cations

As discussed in Section 3.2.3, the interstellar 11.0 μm band is thought to be the cationic counterpart of the 11.2 μm band; e.g., the solo CH_{oop} mode in PAH cations versus PAH neutrals (Rosenberg et al. 2011). In Figure 21, we compare the calculated intensity ratios of the cationic 6.2 μm C–C mode and 11.0 μm solo CH_{oop} mode relative to the 11.2 μm solo CH_{oop} mode in the

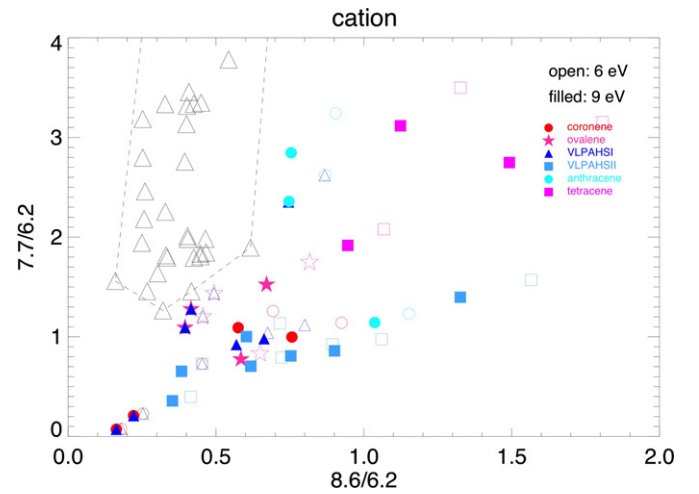


Figure 20. Strength of the 7.7/6.2 vs. 8.6/6.2 μm band strength ratio at two levels of excitation: 6 and 9 eV. The large triangles show the observations, outlined by the dashed outline.

(A color version of this figure is available in the online journal.)

neutral PAH to the observations. A fractional ionization of 0.5 has been assumed. For a different degree of ionization, the calculated values would shift linearly along the indicated line. The observed trend in the calculations reflects the size dependence of the intrinsic strength of the relevant mode and the temperature of the emitting PAH species. The comparison between observations and calculations indicates that for interstellar PAHs, the C–C modes are intrinsically much stronger relative to the CH_{oop} modes than calculated for the cations of this wide range of PAHs. While the observations indicate that neutral PAHs are fully hydrogenated (Hony et al. 2001), this difference suggests that PAH cations are partially dehydrogenated. At any position in the nebula, there will be a rapid exchange between the neutral and cationic PAHs due to photoionization and electron recombination. However, in general, cationic emission will originate from regions which are more exposed to far-ultraviolet photons and hence, perhaps, interstellar cationic PAH spectra might show a higher dehydrogenation fraction. Observationally, there is good evidence for the importance of PAH fragmentation near PDR surfaces where far-ultraviolet fluxes are high and PAH cations dominate (Berné & Tielens 2011).

4.5. Database Fit

Based upon the theoretical spectra calculated for the coronene, ovalene, and irregular PAH families, we have made a least-squares fit to the prototypical, class A, interstellar spectrum of IRAS 23133+6050 (Peeters et al. 2002). This fit is based upon calculated emission spectra that include the full cascade after absorption of an ultraviolet photon. All PAHs are assumed to have absorbed the same photon energy at the beginning of the cascade. This absorbed energy is a free parameter. We have assumed that all bands of all species will be redshifted due to anharmonicity by the same $\Delta\nu_k$, but the value of the shift is left as a free parameter. The intrinsic bands of the emitting PAHs are assumed to be broadened by 16 cm^{-1} . The relative contribution of neutral, cationic, and anionic PAHs is set by the ionization balance, which is determined by the strength of the local ultraviolet field, G_0 , the electron density, n_e , the gas temperature, T , the electron recombination rate coefficient, the ionization rate, and the electron attachment rate coefficient. We have followed the prescription in Tielens (2005) for these

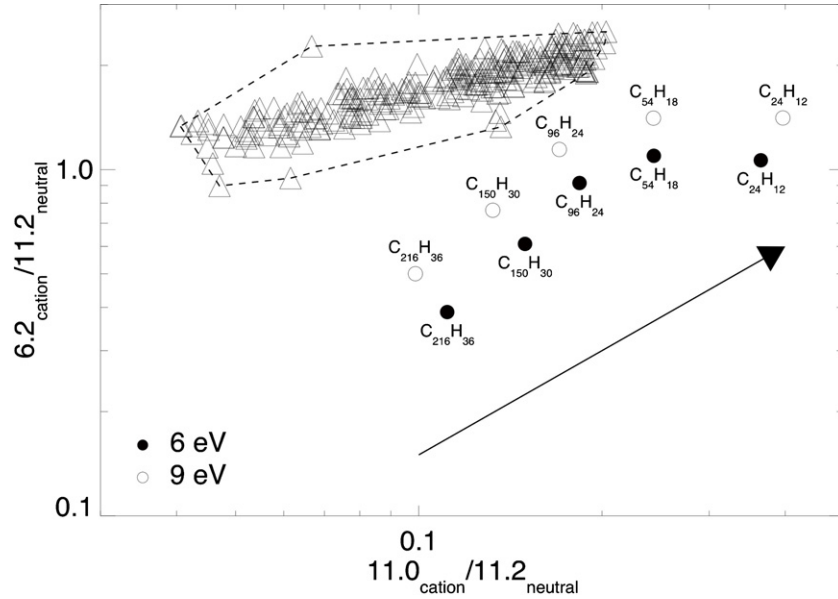


Figure 21. Strength of the 6.2/11.2 vs. 11.0/11.2 μm band strength ratios at two levels of excitation: 6 and 9 eV. The triangles show the observations, outlined by the dashed outline, where the bulk of the astronomical data are taken from Rosenberg et al. 2011. An ionization fraction of 0.5 has been assumed. Adopting other ionization fractions shifts the ratios along a line, indicated by the arrow, through the plotted point and the origin.

Table 3
Flux Contribution in Percent

Species	Anion	Neutral	Cation
$\text{C}_{66}\text{H}_{20}$	0.057	8.1	18
$\text{C}_{96}\text{H}_{24}$	0.038	6.4	18
$\text{C}_{78}\text{H}_{22}$	0.044	6.9	16
$\text{C}_{112}\text{H}_{26}$	0.019	3.5	10
$\text{C}_{24}\text{H}_{12}$	0.037	3.3	4.3
$\text{C}_{120}\text{H}_{36}$	0.005	0.91	2.8
$\text{C}_{150}\text{H}_{30}$	0.00086	0.18	0.65

Note. The final parameters are: $E = 5.7$ eV, $T_{\text{gas}} = 300$ K, $G_0/n_e = 2.93 \times 10^3$, $\text{FWHM} = 16 \text{ cm}^{-1}$ (fixed), and redshift = 21.4 cm^{-1} .

rates. We have adopted a temperature of 300 K—typical for PDRs—and are then left with G_0/n_e as the free parameter describing the (size-dependent) ionization of all species. The fit is compared to the observations in Figure 22 and the flux contribution of the species adding to the emission are given in Table 3. The results for the free parameters in the fit are also reported in the “note” of this table.

The results confirm the conclusions derived in the discussion in the previous sections. The interstellar spectrum is dominated by PAHs with sizes in the range $50 \lesssim N_C \lesssim 110$ (Table 3 and Figure 22). Larger PAHs give negligible contributions. The observed relative strength of the C–H and C–C modes implies about equal contributions by neutrals and cations (Table 3 and Figure 22). The calculated contribution by anions is negligible. The fit is dominated by compact PAHs with long straight edges to account for the strong 11.2 μm band. The 12.7 μm band shows contributions from all of the PAHs in the fit.

Overall, the fit is deemed acceptable but some well-known issues remain. Specifically, the peak position of the 6.2 μm band is not accounted for (no N-substituted PAHs have been included in the fitting procedure). The “7.7” μm band peaks at 7.8 rather than 7.6 μm . The 12.7 μm band occurs at slightly too long a wavelength in the calculations. The 6.2, “7.7,” and 8.6 μm band ratios cannot simultaneously be satisfied. Part of this discrepancy may reflect inherent simplifications, such as

the adopted universal anharmonicity shift. Further laboratory or theoretical studies on the anharmonicity behavior for highly excited PAHs might be fruitful to settle these issues. Other discrepancies indicate that the interstellar PAH family may well be related to the compact PAHs studied here but differs in some key aspects that we do not fully comprehend yet. Further quantum chemical studies along the lines outlined in the previous sections may well be instrumental for further progress in our understanding.

5. SUMMARY AND CONCLUSIONS

Astronomical mid-infrared spectra of a wide variety of objects have revealed a wealth of spectral features. These are now generally attributed to the emission from large (50–100 C-atoms) PAH molecules. In this paper, we have presented the intrinsic infrared characteristics of the coronene family calculated using DFT. By systematically adding rows of hexagons to the PAH species while retaining the overall structure of the molecule, the effect of size on the intrinsic properties of the PAH can be assessed. We have identified trends and derived simple scaling laws for the intrinsic strength of the PAH vibrational modes as a function of size. We have used these data to evaluate the IR emission spectra of such species, taking the energy cascade into account. This study provides new insights into the characteristics of the interstellar PAH family. In addition, the results will be of great use for the development of realistic models of the emission of the interstellar PAH family.

The main conclusions of our work can be summarized as follows.

1. The binding energy per C-atom depends strongly on the PAH structure. Compact PAHs in the coronene and ovalene families are much more stable than less symmetric PAH molecules and may therefore be an important component of the interstellar PAH family.
2. Our calculations confirm and extend conclusions derived from earlier experimental and theoretical studies. Specifically, the detailed vibrational spectrum is sensitive to PAH

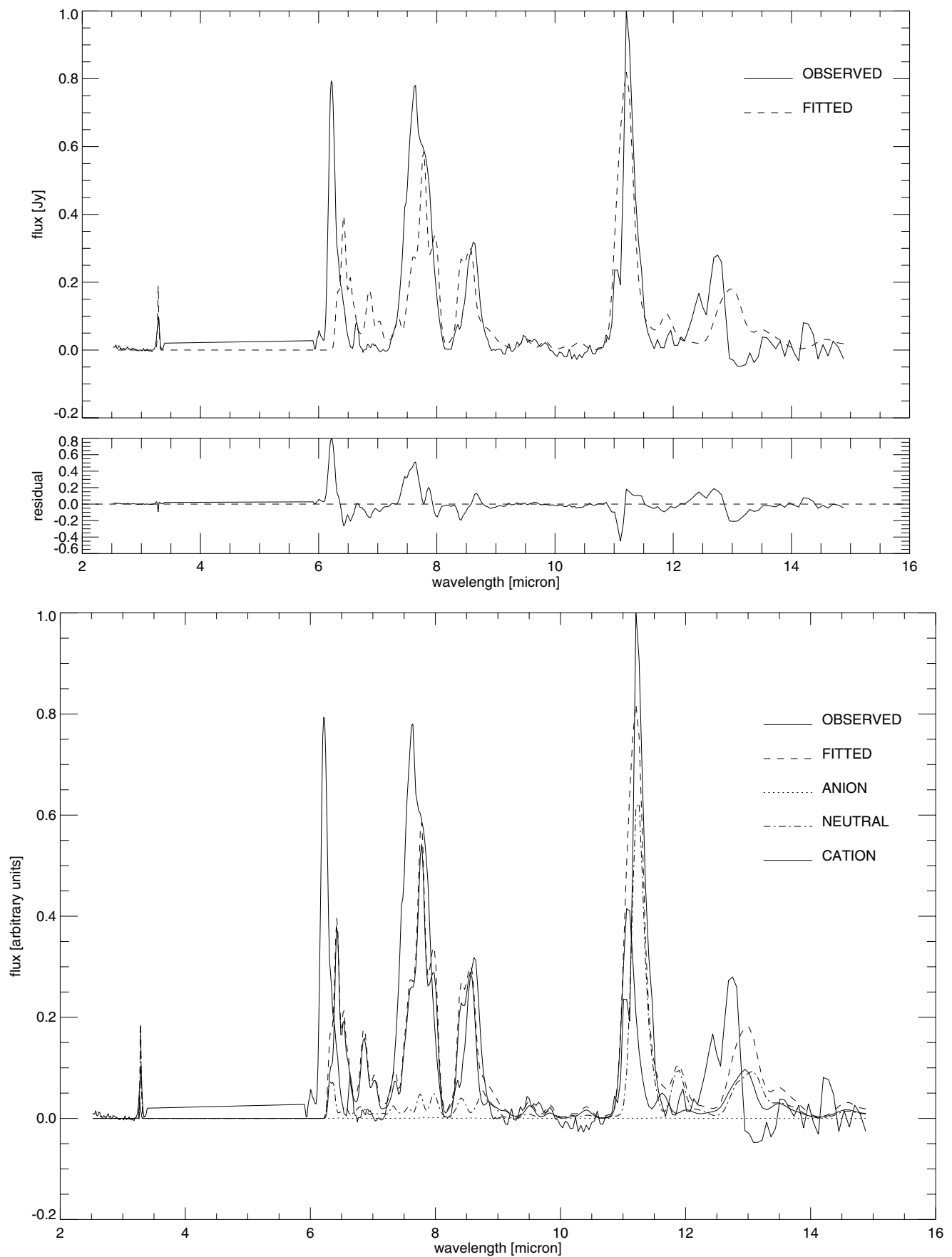


Figure 22. Top: the *ISO-SWS* spectrum of IRAS23133+6050 fitted with the PAHs in the coronene family studied here, utilizing the routines made available through the *AmesPAHdbIDSuite* (Bauschlicher et al. 2010). Bottom: breakdown of the fit into three charge states. Details of the breakdown and the fitted parameters can be found in Table 3.

Table 4

Summary of the Band Positions (in μm), the Total Integrated Intensities (I), and the per H Integrated Intensities ($I(\text{H})$) (in km mol^{-1}) for the Neutrals

Molecule	Intrinsic			Coupled		
	λ	I	$I(\text{H})$	λ	I	$I(\text{H})$
Solo						
C ₅₄ H ₁₈	11.382	64.8	10.8	11.063	220.3	36.7
C ₉₆ H ₂₄	11.084	163.1	13.6	10.957	317.1	26.5
C ₁₅₀ H ₃₀	10.995	264.3	14.7	10.928	398.4	22.1
C ₂₁₆ H ₃₆	10.966	351.4	14.6	10.922	486.3	20.3
C ₂₉₄ H ₄₂	10.959	446.1	14.9	10.927	584.0	19.5
C ₃₈₄ H ₄₈	10.960	550.3	15.3	10.933	704.5	19.6
Duo						
C ₂₄ H ₁₂	11.589					
C ₅₄ H ₁₈	12.259	136.2	11.4	12.804	43.4	3.6
C ₉₆ H ₂₄	12.258	143.9	12.0	12.464	66.1	5.5
C ₁₅₀ H ₃₀	12.309	143.0	11.9	12.744	42.7	3.6
C ₂₁₆ H ₃₆	12.326	149.0	12.4	12.669	52.3	4.4
C ₂₉₄ H ₄₂	12.335	144.0	12.0	12.742	43.3	3.6
C ₃₈₄ H ₄₈	12.335	146.2	12.2	12.715	55.9	4.7
Coupled-mixed Character						
Molecule	λ	I	λ	I	λ	I
C ₁₅₀ H ₃₀	11.738	32.5	13.041	7.4		
C ₂₉₄ H ₄₂	11.311	24.9	12.124	16.6	12.853	7.8
C ₃₈₄ H ₄₈	11.220	16.6	11.840	17.3	13.187	3.3

Note. No redshift is applied.

size and charge state even for PAHs as large as 384 C-atoms. Nevertheless, systematic trends can be discerned.

- We recognize the presence of solo and duo modes in the C–H stretching region and these may be the cause of observed spectral variations in the astronomical 3.3 μm band.
- The pattern of IR-active CC modes in the 6–10 μm region increases rapidly in complexity with size. In addition, the intrinsic strength of the 6.2, 7.7, and 8.6 μm bands show systematic variations with size. The apparent simplicity and the observed relative strength in the astronomical spectra in this wavelength range limit emitting species in the interstellar PAH family to less than ≈ 150 C-atoms.
- Our studies confirm the dependence of the out-of-plane C–H bending modes on the H-adjacency for large PAHs and charge state. In agreement with earlier studies, we attribute the astronomical 11.2 and 11.0 μm bands to the solo mode in neutral and cationic PAHs, respectively. Comparison of model calculations with the observations suggests that the weakness of the 11.0 μm band in astronomical spectra results from severe dehydrogenation of PAH cations.
- The spectra of compact PAHs are much simpler in the 15–20 μm C–C–C region than for non-compact PAHs. As such, compact PAHs are more likely candidates for the observed astronomical bands in this wavelength region.
- Our calculations identify a number of characteristic long-wavelength modes in large PAHs associated with concerted motions. These include the well-known drumhead mode, the jumping-jacks mode, and the in-plane duo-twist mode. The latter two tend to pile up at a specific frequency (220 and 100 cm^{-1}), and these positions are therefore prime targets for astronomical searches of skeletal PAH bands.
- The intrinsic strength of the PAH modes does not scale linearly with the number of C- or H-atoms. Moreover, this dependence is different for different modes and different

charge states. However, for compact PAHs, the derived dependencies are not very sensitive to the molecular geometry.

- As for small PAHs, model calculations of the IR emission show that the C–H modes can still largely be ascribed to neutral PAHs while the C–C modes are due primarily to cationic PAHs.
- Our studies validate the use of the 3.3/11.2 μm band ratio as a measure of the size of the emitting PAHs over the full size range studied (24–384 C-atoms).
- A least-squares fit to the observed spectrum based upon the calculated IR emission spectra of PAHs confirms the conclusions derived from our analysis.

A.R. thanks NASA's Astrophysics Theory and Fundamental Physics (ATFP; NNX09AD18G) program for its generous support of this work. We also acknowledge support from NASA Astrobiology and Laboratory Astrophysics programs. This work was supported through an appointment (C.B.) to the NASA Post-doctoral Program at the Ames Research Center, administered by Oak Ridge Associated Universities through a contract with NASA. Studies of interstellar PAHs at Leiden Observatory are supported through advanced-ERC grant 246976 from the European Research Council and through the Dutch Astrochemistry Network funded by the Dutch Science Organization, NWO.

APPENDIX

In previous work, Bauschlicher et al. (2008, 2009) noted the coupling between the solo and duo bands. Given the large range in size of the molecules considered in this work, it is now possible to investigate how this coupling changes as a function of PAH size. To evaluate the coupling between solos and duos, the mass of either the solo or duo hydrogens is changed from 1.00783 (hydrogen) to 0.2 amu. This change in mass shifts the CH_{oop} modes out of the 10–15 μm region and eliminates the solo–duo coupling, which allows us to determine the *intrinsic* band positions and intensities of the solos and duos bands, which are listed in Table 4 for the neutrals and in Table 5 for the ions. The spectra with and without the decoupling of the solo and duo hydrogens for C₅₄H₁₈ and C₃₈₄H₄₈ are shown in Figures 7 and 8. The solo *intrinsic* (no coupling with duos) total intensity (I) and the *intrinsic* intensity per C–H ($I(\text{CH})$) increase systematically with size as the number of solo hydrogens increases and the solos couple among themselves. The band position of the *intrinsic* solos shifts to shorter wavelength with size and converges to 10.96 μm . It is interesting to note that the *intrinsic* solo band converges more slowly than the coupled solo band. The duo *intrinsic* intensities reflect the strength of the duo motion without the solo coupling. The values are not dependent on the PAH size, as the number of duos is 12 for all the PAHs considered in this work. The band position of the *intrinsic* duos shifts to longer wavelength with size and converges to 12.34 μm . By comparing the *intrinsic* and *coupled* results, we can deduce the effect of the solo–duo coupling; the solo band position shifts to shorter wavelength, whereas the duo band position shifts to longer wavelength. The total intensity and the intensity per C–H increase significantly for the solo hydrogens, whereas the total intensity and the intensity per C–H decrease for the duos. The strength of the coupling between solo and duo hydrogens depends on the ratio of the number of solos to the number of duos. The number of duos is constant for our series of very compact PAHs, whereas the number of solos steadily increases. Therefore, the number of duos available to couple with solos

Table 5

Summary of the Band Positions (in μm), the Total Integrated Intensities (I), and the per H Integrated Intensities ($I(\text{H})$) (in km mol^{-1}) for the Ions

Molecule	Intrinsic			Coupled		
	λ	I	$I(\text{H})$	λ	I	$I(\text{H})$
Solo						
C ₅₄ H ₁₈ ⁺	11.194	59.9	10.0	10.880	220.4	36.7
C ₉₆ H ₂₄ ⁺	10.946	155.1	12.9	10.821	297.5	24.8
C ₁₅₀ H ₃₀ ⁺	10.890	246.2	13.7	10.825	380.2	21.1
C ₂₁₆ H ₃₆ ⁺	10.900	335.0	14.0	10.857	471.7	19.7
C ₅₄ H ₁₈ ⁻	11.980	61.0		11.362	133.9	22.2
	11.472	11.6				
C ₉₆ H ₂₄ ⁻	11.421	138.8		11.329	155.3	
	11.176	34.0		11.133	163.6	
C ₁₅₀ H ₃₀ ⁻	11.230	270.2	15.0	11.074	412.9	22.9
C ₂₁₆ H ₃₆ ⁻	11.147	368.8	15.4	11.072	512.2	21.3
Mixed Character						
C ₅₄ H ₁₈ ⁺				12.666	54.1	
C ₁₅₀ H ₃₀ ⁺				11.633	37.6	
C ₂₁₆ H ₃₆ ⁺				11.395	34.9	
C ₅₄ H ₁₈ ⁻				11.703	101.8	
C ₁₅₀ H ₃₀ ⁻				11.909	23.6	
C ₂₁₆ H ₃₆ ⁻				11.602	12.1	
Duo						
C ₅₄ H ₁₈ ⁺	12.151	145.5	12.1	12.222	1.2	0.1
C ₉₆ H ₂₄ ⁺	12.188	150.1	12.5	12.382	76.7	6.4
C ₁₅₀ H ₃₀ ⁺	12.240	147.5	12.3	12.657	48.5	4.0
C ₂₁₆ H ₃₆ ⁺	12.264	146.9	12.2	12.604	55.7	4.7
C ₅₄ H ₁₈ ⁻	12.477	134.4	11.2	13.137	23.6	2.0
C ₉₆ H ₂₄ ⁻	12.370	141.2	11.8	12.596	50.5	4.2
C ₁₅₀ H ₃₀ ⁻	12.366	141.3	11.8	12.868	33.4	2.8
C ₂₁₆ H ₃₆ ⁻	12.359	142.0	11.8	12.718	47.7	4.0

Note. No redshift is applied.

decreases with size and the strength of the solo–duo coupling decreases with PAH size. The solo-coupled band positions shift to shorter wavelength as the PAH size increases. The magnitude of the band position shift reflects the strength of the solo–duo coupling. In addition to shifting the band positions, the coupling can split the duo band into more than one band and produce additional bands that are mixed in character.

REFERENCES

Allamandola, L. J., Hudgins, D. M., & Sandford, S. A. 1999, *ApJ*, **511**, L115
 Allamandola, L. J., Tielens, A. G. G. M., & Barker, J. R. 1985, *ApJ*, **290**, L25
 Allamandola, L. J., Tielens, A. G. G. M., & Barker, J. R. 1989, *ApJS*, **71**, 733
 Armus, L., Charmandaris, V., Bernard-Salas, J., et al. 2007, *ApJ*, **656**, 148
 Barker, J. R., Allamandola, L. J., & Tielens, A. G. G. M. 1987, *ApJ*, **315**, L61
 Barone, V. 2005, *J. Chem. Phys.*, **122**, 014108
 Bauschlicher, C. W., Boersma, C., Ricca, A., et al. 2010, *ApJS*, **189**, 341
 Bauschlicher, C. W., & Langhoff, S. R. 1997, *Spectrochim. Acta A*, **53**, 1225
 Bauschlicher, C. W., Peeters, E., & Allamandola, L. J. 2008, *ApJ*, **678**, 316
 Bauschlicher, C. W., Peeters, E., & Allamandola, L. J. 2009, *ApJ*, **697**, 311
 Becke, A. D. 1993, *J. Chem. Phys.*, **98**, 5648
 Berné, O., Joblin, C., Deville, Y., et al. 2007, *A&A*, **469**, 575
 Berné, O., & Tielens, A. G. G. M. 2011, *Proc. Natl Acad. Sci. USA*, **109**, 401
 Boersma, C., Bauschlicher, C. W., Allamandola, L. J., et al. 2010, *A&A*, **511**, A32
 Boersma, C., Bauschlicher, C. W., Ricca, A., et al. 2011, *ApJ*, **729**, 64
 Bregman, J. D., Allamandola, L. J., Witteborn, F. C., Tielens, A. G. G. M., & Geballe, T. R. 1989, *ApJ*, **344**, 791
 Cami, J., Bernard-Salas, J., Peeters, E., & Malek, S. E. 2010, *Science*, **329**, 1180
 Candian, A., Kerr, T. H., Song, I.-O., McCombie, J., & Sarre, P. 2012, *MNRAS*, in press
 Clar, E. 1972, *The Aromatic Sextet* (London: Wiley)
 Cook, D. J., Schlemmer, S., Balucani, N., et al. 1998, *J. Phys. Chem.*, **102**, 1467

de Frees, D. J., Miller, M. D., Talbi, D., Pauzat, F., & Ellinger, Y. 1993, *ApJ*, **408**, 530
 Desert, F.-X., Boulanger, F., & Puget, J. L. 1990, *A&A*, **237**, 215
 Draine, B. T., & Li, A. 2001, *ApJ*, **551**, 807
 Draine, B. T., & Li, A. 2007, *ApJ*, **657**, 810
 Engelbracht, C. W., Kundurthy, P., Gordon, K. D., et al. 2006, *ApJ*, **642**, L127
 Frisch, M. J., Pople, J. A., & Binkley, J. S. 1984, *J. Chem. Phys.*, **80**, 3265
 Frisch, M. J., Trucks, G. W., Schlegel, H. B., et al. 2009, Gaussian 09, Revision A.02 (Wallingford, CT: Gaussian, Inc.)
 Geballe, T. R., Tielens, A. G. G. M., Allamandola, L. J., Moorhouse, A., & Brand, P. W. J. L. 1989, *ApJ*, **341**, 278
 Hony, S., van Kerckhoven, C., Peeters, E., et al. 2001, *A&A*, **370**, 1030
 Hudgins, D. M., & Allamandola, L. J. 1995, *J. Phys. Chem.*, **99**, 3033
 Hudgins, D. M., & Allamandola, L. J. 1999a, *ApJ*, **516**, L41
 Hudgins, D. M., & Allamandola, L. J. 1999b, *ApJ*, **513**, L69
 Hudgins, D. M., Bauschlicher, C. W., & Allamandola, L. J. 2005, *ApJ*, **632**, 316
 Hudgins, D. M., Bauschlicher, C. W., & Sandford, S. A. 2004, *ApJ*, **614**, 770
 Huneycutt, A. J., Casaes, R. N., McCall, B. J., et al. 2004, *Chem. Phys. Chem.*, **5**, 321
 Joblin, C., Boissel, P., Leger, A., D'Hendecourt, L., & Defourneau, D. 1995, *A&A*, **299**, 835
 Joblin, C., Mulas, G., Mallocci, G., & Bergin, E. 2011, in *In PAHs and the Universe: A Symposium to Celebrate the 25th Anniversary of the PAH Hypothesis*, EAS Publications Series, ed. A. G. G. M. Tielens & C. Joblin (Cambridge: Cambridge University Press), 46, 123
 Joblin, C., Toubanc, D., Boissel, P., & Tielens, A. G. G. M. 2002, *Mol. Phys.*, **100**, 3595
 Kim, H.-S., Wagner, D. R., & Saykally, R. J. 2001, *Phys. Rev. Lett.*, **86**, 5691
 Knorke, H., Langer, J., Oomens, J., & Dopfer, O. 2009, *ApJ*, **706**, L66
 Langhoff, S. R. 1996, *J. Phys. Chem.*, **100**, 2819
 Leach, S. 1989, in *IAU Symp. 135, Interstellar Dust*, ed. L. J. Allamandola & A. G. G. M. Tielens (Dordrecht: Kluwer), 155
 Léger, A., & Puget, J. L. 1984, *A&A*, **137**, L5
 Low, F. J., Young, E., Beintema, D. A., et al. 1984, *ApJ*, **278**, L19
 Mallocci, G., Cappellini, G., Mulas, G., & Matoni, A. 2011, *Chem. Phys.*, **384**, 19
 Mallocci, G., Joblin, C., & Mulas, G. 2007, *Chem. Phys.*, **332**, 353
 Mattioda, A. L., Hudgins, D. M., & Allamandola, L. J. 2005, *ApJ*, **629**, 1188
 Mattioda, A. L., Ricca, A., Tucker, J., Bauschlicher, C. W., & Allamandola, L. J. 2009, *ApJ*, **137**, 4054
 Meeus, G., Waters, L. B. F. M., Bouwman, J., et al. 2001, *A&A*, **365**, 476
 Micelotta, E. R., Jones, A. P., & Tielens, A. G. G. M. 2010, *A&A*, **510**, A36
 Moutou, C., Leger, A., & D'Hendecourt, L. 1996, *A&A*, **310**, 297
 Moutou, C., Sellgren, K., Leger, A., et al. 1998, in *ASP Conf. Ser. 132, Star Formation with the Infrared Space Observatory*, ed. J. Yun & L. Liseau (San Francisco, CA: ASP), 47
 Moutou, C., Sellgren, K., Verstraete, L., & Léger, A. 1999, *A&A*, **347**, 949
 Moutou, C., Verstraete, L., Léger, A., Sellgren, K., & Schmidt, W. 2000, *A&A*, **354**, L17
 Mulas, G., Mallocci, G., Joblin, C., & Toubanc, D. 2006a, *A&A*, **460**, 93
 Mulas, G., Mallocci, G., Joblin, C., & Toubanc, D. 2006b, *A&A*, **456**, 161
 Mulas, G., Mallocci, G., Joblin, C., Toubanc, D., & Porceddu, I. 2005, in *Proc. Dusty and Molecular Universe: A Prelude to Herschel and ALMA*, ed. A. Wilson (ESA Special Publication, Vol. 577; Noordwijk: ESA), 395
 Oomens, J. 2011, in *In PAHs and the Universe: A Symposium to Celebrate the 25th Anniversary of the PAH Hypothesis*, EAS Publications Series, ed. A. G. G. M. Tielens & C. Joblin (Cambridge: Cambridge University Press), 46, 61
 Oomens, J., Sartakov, B. G., Tielens, A. G. G. M., Meijer, G., & von Helden, G. 2001, *ApJ*, **560**, L99
 Oomens, J., Tielens, A. G. G. M., Sartakov, B. G., von Helden, G., & Meijer, G. 2003, *ApJ*, **591**, 968
 Pathak, A., & Rastogi, S. 2007, *Spectrochim. Acta A*, **67**, 898
 Pauzat, F., Pilmé, J., Toulouse, J., & Ellinger, Y. 2010, *J. Chem. Phys.*, **133**, 054301
 Pauzat, F., Talbi, D., & Ellinger, Y. 1997, *A&A*, **319**, 318
 Pech, C., Joblin, C., & Boissel, P. 2002, *A&A*, **388**, 639
 Peeters, E., Hony, S., van Kerckhoven, C., et al. 2002, *A&A*, **390**, 1089
 Piest, H., von Helden, G., & Meijer, G. 1999, *ApJ*, **520**, L75
 Pino, T., Dartois, E., Cao, A.-T., et al. 2008, *A&A*, **490**, 665
 Platt, J. R. 1956, *ApJ*, **123**, 486
 Portmann, S., & Lüthi, H. P. 2000, *CHIMIA Int. J. Chem.*, **54**, 766
 Puget, J. L., & Léger, A. 1989, *ARA&A*, **27**, 161
 Rapacioli, M., Joblin, C., & Boissel, P. 2005, *A&A*, **429**, 193
 Regan, M. W., Thornley, M. D., Bendo, G. J., et al. 2004, *ApJS*, **154**, 204
 Ricca, A., Bauschlicher, C. W., Jr., & Allamandola, L. J. 2011a, *ApJ*, **727**, 128
 Ricca, A., Bauschlicher, C. W., Jr., & Allamandola, L. J. 2011b, *ApJ*, **729**, 94

- Ricca, A., Bauschlicher, C. W., Jr., Mattioda, A. L., Boersma, C., & Allamandola, L. J. 2010, *ApJ*, **709**, 42
- Robertson, J. 2002, *Mater. Sci. Eng.*, **R37**, 129
- Rosenberg, M. J. F., Berné, O., Boersma, C., Allamandola, L. J., & Tielens, A. G. G. M. 2011, *A&A*, **532**, A128
- Schlemmer, S., Cook, D. J., Harrison, J. A., et al. 1994, *Science*, **265**, 1686
- Schmidt, T. W., Pino, T., & Bréchnignac, P. 2009, *J. Phys. Chem. A*, **113**, 3535
- Schutte, W. A., Tielens, A. G. G. M., & Allamandola, L. J. 1993, *ApJ*, **415**, 397
- Sellgren, K. 1984, *ApJ*, **277**, 623
- Sellgren, K., Uchida, K. I., & Werner, M. W. 2007, *ApJ*, **659**, 1338
- Sellgren, K., Werner, M. W., Ingalls, J. G., et al. 2010, *ApJ*, **722**, L54
- Shida, T., & Iwata, S. 1973, *J. Am. Chem. Soc.*, **95**, 3473
- Sloan, G. C., Jura, M., Duley, W. W., et al. 2007, *ApJ*, **664**, 1144
- Sloan, G. C., Keller, L. D., Forrest, W. J., et al. 2005, *ApJ*, **632**, 956
- Smith, J. D. T., Draine, B. T., Dale, D. A., et al. 2007, *ApJ*, **656**, 770
- Song, I.-O., McCombie, J., Kerr, T. H., & Sarre, P. J. 2007, *MNRAS*, **380**, 979
- Stein, S. E. 1978, *J. Phys. Chem.*, **82**, 566
- Stein, S. E., & Brown, R. L. 1987, *J. Am. Chem. Soc.*, **109**, 3721
- Stephens, P. J., Devlin, F. J., Chabalowski, C. F., & Frisch, M. J. 1994, *J. Phys. Chem.*, **98**, 11623
- Szczepanski, J., & Vala, M. 1993a, *ApJ*, **414**, 646
- Szczepanski, J., & Vala, M. 1993b, *Nature*, **363**, 699
- Tielens, A. G. G. M. 2005, *The Physics and Chemistry of the Interstellar Medium* (Cambridge: Cambridge Univ. Press)
- Tielens, A. G. G. M. 2008, *ARA&A*, **46**, 289
- Tokunaga, A. T., Sellgren, K., Smith, R. G., et al. 1991, *ApJ*, **380**, 452
- van Dienenhoven, B., Peeters, E., van Kerckhoven, C., et al. 2004, *ApJ*, **611**, 928
- van Kerckhoven, C., Hony, S., Peeters, E., et al. 2000, *A&A*, **357**, 1013
- Van-Oahn, N.-T., Falvo, C., Lauvergnat, D., et al. 2012, *Phys. Chem. Chem. Phys.*, **14**, 2381
- Verstraete, L., Puget, J. L., Falgarone, E., et al. 1996, *A&A*, **315**, L337
- Wehres, N., Romanzin, C., Linnartz, H., van Winckel, H., & Tielens, A. G. G. M. 2010, *A&A*, **518**, A36
- Werner, M. W., Uchida, K. I., Sellgren, K., et al. 2004, *ApJS*, **154**, 309